J. Fluid Mech. (2016), *vol.* 800, *pp.* 531–556. © Cambridge University Press 2016
doi:10.1017/jfm.2016.411

The effect of thermal boundary conditions on forced convection heat transfer to fluids at supercritical pressure

Hassan Nemati[1], Ashish Patel[1], Bendiks J. Boersma[1] and Rene Pecnik[1,†]

[1]Process and Energy Department, Delft University of Technology, Leeghwaterstraat 39, 2628 CB Delft, The Netherlands

(Received 30 October 2015; revised 23 May 2016; accepted 13 June 2016; first published online 12 July 2016)

We use direct numerical simulations to study the effect of thermal boundary conditions on developing turbulent pipe flows with fluids at supercritical pressure. The Reynolds number based on pipe diameter and friction velocity at the inlet is $Re_{\tau 0} = 360$ and Prandtl number at the inlet is $Pr_0 = 3.19$. The thermodynamic conditions are chosen such that the temperature range within the flow domain incorporates the pseudo-critical point where large variations in thermophysical properties occur. Two different thermal wall boundary conditions are studied: one that permits temperature fluctuations and one that does not allow temperature fluctuations at the wall (equivalent to cases where the thermal effusivity ratio approaches infinity and zero, respectively). Unlike for turbulent flows with constant thermophysical properties and Prandtl numbers above unity – where the effusivity ratio has a negligible influence on heat transfer – supercritical fluids shows a strong dependency on the effusivity ratio. We observe a reduction of 7 % in Nusselt number when the temperature fluctuations at the wall are suppressed. On the other hand, if temperature fluctuations are permitted, large property variations are induced that consequently cause an increase of wall-normal velocity fluctuations very close to the wall and thus an increased overall heat flux and skin friction.

Key words: pipe flow boundary layer, turbulence simulation, turbulent flows

1. Introduction

There has been a considerable interest in utilising fluids at pressures and temperatures above their vapour–liquid critical point in many industrial applications. Supercritical fluids exhibit significant deviations from ideal thermodynamic behaviour and do not undergo vaporisation or condensation phase transitions. Supercritical fluid-based technologies are involved in a wide variety of technical process such as pharmaceutical processes for the formation of micro and nanoparticles (Fages *et al.* 2004) and in chemical engineering as solvents (Matson *et al.* 1987*a*; Matson, Petersen & Smith 1987*b*; Debenedetti *et al.* 1993). Due to their peculiar thermodynamic properties, they are also used in energy applications, such as heat pumps, refrigeration

† Email address for correspondence: r.pecnik@tudelft.nl

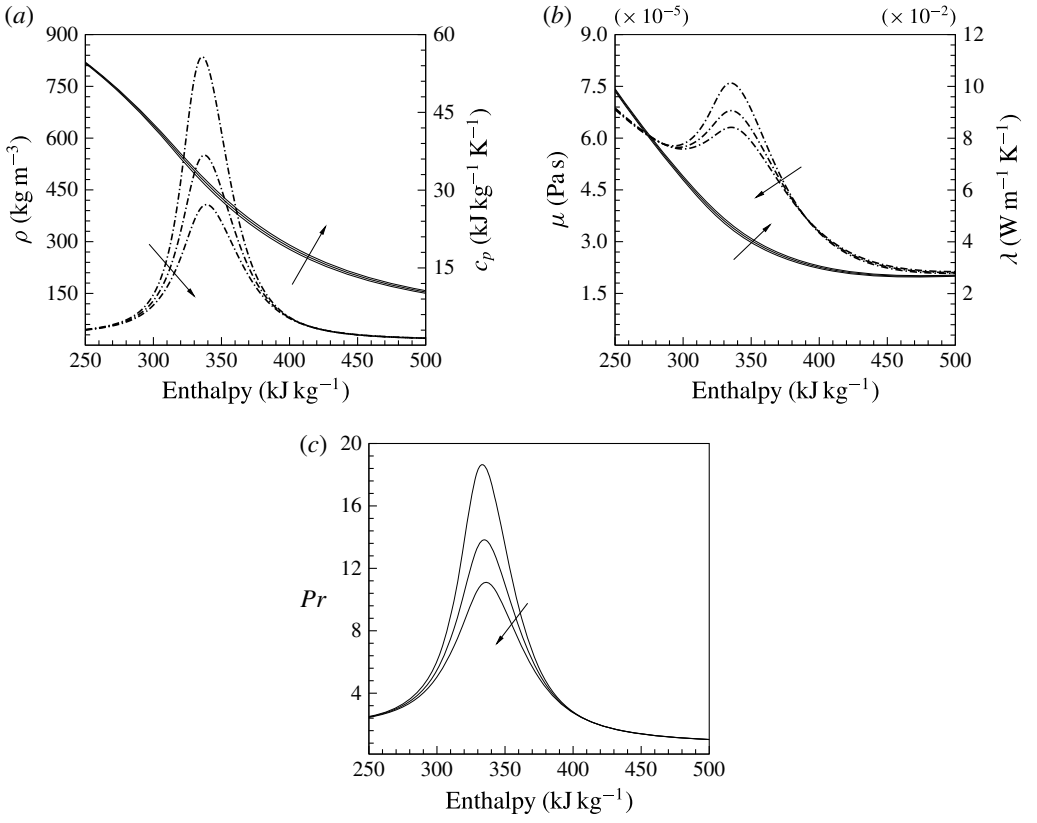

FIGURE 1. Property variations of carbon dioxide CO_2 versus enthalpy for pressures $P_0 = 78$, 80 and 82 bar based on Span & Wagner (2003) (arrows show the direction of increasing P_0). (*a*) Density ρ (——) and isobaric heat capacity c_p (— · —), (*b*) dynamic viscosity μ (——) and thermal conductivity λ (— · —) and (*c*) Prandtl number (——).

cycles (Ma, Liu & Tian 2013), power cycles (Dostal, Hejzlar & Driscoll 2006; Chen, Goswami & Stefanakos 2010) and biodiesel production (Saka & Kusdiana 2001).

In the supercritical region, small changes in temperature and pressure can lead to substantial changes in thermophysical properties. As an example, figure 1 shows the variation of thermophysical properties of CO_2 as a function of temperature at three different pressures above the critical pressure ($P_{critical} = 73.773$ bar). It shows that the thermophysical properties of the fluid, at constant pressure, vary significantly within a narrow temperature range (295–355 K) across the pseudo-critical temperature T_{pc}. The pseudo-critical temperature T_{pc} is defined as the temperature along a supercritical isobar at which the specific heat capacity c_p has a maximum value. This is also the point where a supercritical isobar intersects with the critical isochore (density at the critical point). Owing to these unusual thermophysical properties, heat transfer at a supercritical pressure is very different from that at subcritical pressures. Experimental and numerical studies of heat transfer characteristics of flows at supercritical pressure have been reviewed by Yoo (2013) and detailed turbulence statistics containing second-order moments for Reynolds stresses and turbulent heat flux obtained from direct numerical simulation (DNS) are given in Bae, Yoo & Choi (2005), Bae, Yoo & McEligot (2008) and Nemati *et al.* (2015). It was shown that property fluctuations, in

the case of an isoflux wall boundary condition, significantly affect the mean energy transfer and strongly modify the average heat flux distribution at, and close to, the wall. This motivated us to study the effect of the thermal effusivity ratio on heat transfer to supercritical fluids.

The thermal effusivity ratio K (also called the thermal activity ratio) describes the ability of two materials to exchange heat. The thermal effusivity is defined as the square root of the product of density, thermal conductivity and specific heat capacity, namely $e = \sqrt{\rho\lambda c_p}$ (Carslaw & Jaeger 1959). For example, if two semi-infinite materials with different temperatures T_1 and T_2 are brought into contact, the equilibrium contact temperature is a function of $K = e_2/e_1$, expressed as $T_c = (T_1 + KT_2)/(1 + K)$. It follows that for $K \gg 1$, the contact temperature is closer to T_2, while for $K \ll 1$ it is closer to T_1. In the case of heat transfer between a turbulent flow and a solid, the thermal effusivity ratio ($K = e_{fluid}/e_{solid}$) not only determines the averaged contact temperature but also whether wall temperature fluctuations are allowed or suppressed. Kasagi, Kuroda & Hirata (1989) investigated the effect of thermal effusivity ratio, wall thickness, and Prandtl number on wall temperature fluctuations and turbulent heat transfer. They found that for thick solid walls and $K \to 0$, no temperature fluctuations can occur, such that the thermal boundary condition can be approximated as an ideal isothermal wall. This condition is met for combinations of air and most solid materials, and for water if heated or cooled by a thick copper wall. On the other hand, for $K \to \infty$ the wall heat flux can be described by an ideal isoflux wall boundary condition. For values of $K \approx 1$, such as water and glass, temperature fluctuations at the wall are approximately 50 % to that of an ideal isoflux wall. Kasagi *et al.* (1989) also investigated the effect of wall thickness on temperature fluctuations. For fluids with $Pr \approx 1$ and a thermal conductivity a hundred times lower than that of the solid, temperature fluctuations are independent for wall thicknesses larger than the non-dimensional wall distance of $y^+ \approx 100$ of the fluid. By decreasing the wall thickness, the temperature fluctuations approach the value of the ideal isoflux condition, even for $K \ll 1$. Later, Tiselj *et al.* (2001*a*) confirmed the results of Kasagi *et al.* (1989) by performing DNS of fully developed turbulent channel flows with conjugate heat transfer by varying values of wall thickness, effusivity ratio and Prandtl number.

Kays & Crawford (1993) found that in a fully developed turbulent pipe flow the effects of temperature fluctuations on heat transfer vanish with increasing Prandtl number and that the Nusselt number for isoflux and isothermal boundary conditions are equal if $Pr \geqslant 0.7$. This can be explained by the thickness of thermal resistance region, which depends on the Prandtl number. For fluids with $Pr \ll 1$ the dominant heat transfer mechanism is thermal conduction, which causes the thermal resistance region to move toward the centre of the pipe. In this case, different thermal wall boundary conditions have a large influence on temperature fluctuations and consequently heat transfer from the wall. A higher value of Pr causes the thermal resistance region to move closer to the wall, such that the vanishing (small) velocity fluctuations very close to the wall mitigate the effect of temperature fluctuations on the wall-normal turbulent heat flux. Studies on flat plate boundary layers with respect to different thermal boundary conditions were performed by Kong, Choi & Lee (2000) and Li *et al.* (2009). They showed that close to the wall the behaviour of the wall-normal heat flux for isothermal wall boundary conditions is similar to that of the Reynolds shear stress, implying consistency between temperature and streamwise velocity. They also confirmed that the mean temperature profiles and the streamwise Stanton number ($St = Nu/(Re\,Pr)$) distributions are independent of the boundary

condition for Prandtl numbers above unity. Further studies on this topic have been performed by Iritani, Kasagi & Hirata (1985), Hetsroni & Rozenblit (1994), Mosyak, Pogrebnyak & Hetsroni (2001), Verzicco & Sreenivasan (2008), who also investigated the effect of thermal wall boundary condition on wall temperature fluctuations and turbulent heat transfer.

In this work, we investigate the influence of thermal wall boundary conditions, namely isothermal ($K \to 0$) and isoflux ($K \to \infty$), on heat transfer to fluids with large property variations and high Prandtl numbers. The configuration is a heated developing pipe flow with supercritical CO_2 at a pressure of 80 bar. The fluid temperature at the inlet is slightly below the thermodynamic pseudo-critical point and the fluid is heated at the wall, such that the fluid crosses a region where strong thermophysical property variations occur. If supercritical CO_2 at 80 bar is considered as the heat transfer medium in a heat exchanger made of stainless steel, the effusivity ratio at the pseudo-critical temperature is of the order of $K = 0.15$. Thus, it can be expected that considerable temperature fluctuations at the wall can occur, which can be estimated to approximately 20 % that of ideal isoflux boundary conditions for thick walls (see, for example, Kasagi *et al.* 1989; Tiselj *et al.* 2001*a*; Tiselj & Cizelj 2012). For thin walls, the fluctuations can be even higher. However, the Prandtl number close to the pseudo-critical point is approximately 14 (see figure 1) and the effect of the thermal boundary conditions – and thus wall temperature fluctuations – on the turbulent heat transfer should be negligible. As we will outline in this work, this is not the case for fluids with large property variations.

The organisation of the paper is as follows. In § 2 the governing equations of momentum and energy in their low Mach number approximation are briefly described and §§ 3 and 4 discuss the simulation set-up and boundary conditions. Section 5 outlines the results for the instantaneous fields (§ 5.1), mean and turbulence statistics (§ 5.2), quadrant analysis of the Reynolds shear stress and the turbulent heat flux (§ 5.3) and turbulence budgets in § 5.4. In § 5.5 we exploit the Fukagata, Iwamoto & Kasagi identity (Fukagata, Iwamoto & Kasagi 2002) to show the exact relations between wall quantities, e.g. wall shear stress and wall heat flux, and the contributions from different physical mechanisms. The summary of our results is given in § 6.

2. Governing equations

In the present study, the anelastic (also known as the low Mach number) approximation of the Navier–Stokes equations in cylindrical coordinates is solved. The effects associated with density changes in response to pressure fluctuations, which are regarded as compressibility effects, are thus not captured. However, the variable inertia effects related to density changes due to heat transfer are taken into account (Lele 1994). For the sake of brevity, the derivation of the governing equations is omitted and can be found in Nemati *et al.* (2015). The final form of the equations is:

$$\frac{\partial \rho}{\partial t} + \frac{\partial \rho u_i}{\partial x_i} = 0, \tag{2.1}$$

$$\frac{\partial \rho u_i}{\partial t} + \frac{\partial \rho u_i u_j}{\partial x_j} = -\frac{\partial p}{\partial x_i} + \frac{1}{Re_{\tau 0}} \frac{\partial \tau_{ij}}{\partial x_j}, \tag{2.2}$$

$$\frac{\partial \rho h}{\partial t} + \frac{\partial \rho u_i h}{\partial x_i} = -\frac{1}{Re_{\tau 0} Pr_0} \frac{\partial q_i}{\partial x_i}, \tag{2.3}$$

where $\tau_{ij} = 2\mu S_{ij} = \mu(\partial u_i/\partial x_j + \partial u_j/\partial x_i - 2/3\,\partial u_k/\partial x_k \delta_{ij})$ is the stress tensor, $q_i = -\lambda \partial T/\partial x_i = -\alpha \partial h/\partial x_i$ is the Fourier law for the heat conduction and δ_{ij} is the Kronecker delta. Note, the Fourier law can be also expressed in terms of the enthalpy as, $q_i = -\alpha \partial h/\partial x_i$, with $c_p = \partial h/\partial T$ and $\alpha = \lambda/c_p$. The symbols t, x_i, ρ, μ, λ, c_p, u_i, T, p and h are the dimensionless time, coordinates, density, dynamic viscosity, thermal conductivity, isobaric heat capacity, velocity, temperature, hydrodynamic pressure and enthalpy, respectively. These quantities are non-dimensionalised as:

$$\left.\begin{aligned} t = \frac{t^*}{D^*/u^*_{\tau 0}}, \quad x_i = \frac{x_i^*}{D^*}, \quad \rho = \frac{\rho^*}{\rho_0^*}, \quad \mu = \frac{\mu^*}{\mu_0^*}, \quad \lambda = \frac{\lambda^*}{\lambda_0^*}, \\ c_p = \frac{c_p^*}{c_{p0}^*}, \quad u_i = \frac{u_i^*}{u_{\tau 0}^*}, \quad T = \frac{T^*}{T_0^*}, \quad p = \frac{p^*}{\rho_0^* u_{\tau 0}^{*2}}, \quad h = \frac{h^* - h_0^*}{c_{p0}^* T_0^*}. \end{aligned}\right\} \tag{2.4}$$

Here, the superscript * denotes the dimensional quantities and the subscript $_0$ denotes the values at the pipe inlet. The non-dimensional numbers are given by

$$Re_{\tau 0} = \frac{\rho_0^* u_{\tau 0}^* D^*}{\mu_0^*}, \quad Pr_0 = \frac{\mu_0^* c_{p0}^*}{\lambda_0^*}, \quad Q = \frac{q_w^* D^*}{\lambda_0^* T_0^*}, \tag{2.5a–c}$$

with $Re_{\tau 0}$ the Reynolds number based on the inlet friction velocity and the pipe diameter D^*, Pr_0 is the inlet Prandtl number, Q is the non-dimensional constant wall heat flux and q_w^* is the dimensional constant wall heat flux.

3. Thermal boundary conditions and simulation set-up

Before we discuss the numerical details and the results, it is necessary to outline the procedure for setting the thermal boundary conditions in our simulations. The aim of this work is to investigate the effect of wall temperature fluctuations on the Nusselt number for flows with variable thermophysical properties. Therefore, it is crucial that the thermodynamic conditions for all the investigated cases are equivalent, such that the observed effects on heat transfer only depend on wall temperature fluctuations and not on different thermodynamic states (note, the thermophysical properties depend on the absolute value of temperature).

Kong *et al.* (2000) and Li *et al.* (2009) investigated the effect of zero/non-zero wall temperature fluctuations on the Nusselt number for constant property fluids by setting isothermal and isoflux boundary condition, respectively. The Nusselt number is defined as $Nu = HL^*_{ref}/\lambda^*_{ref}$, with the heat transfer coefficient H, a reference length L^*_{ref} and a reference thermal conductivity λ^*_{ref} of the fluid. In their simulations, the non-dimensional temperature Θ, the thermal wall boundary condition, and the Nusselt number Nu for $K \to 0$ and $K \to \infty$ can be summarised as follows,

$$K \to 0: \quad \Theta = (T_w^* - T^*)/(T_w^* - T_\infty^*), \quad \Theta|_w = 0, \quad Nu = \partial\overline{\Theta}/\partial y|_w, \tag{3.1a–c}$$

$$K \to \infty: \quad \Theta = (T_\infty^* - T^*)/(q_w^* L^*_{ref}/\lambda^*_{ref}), \quad \partial\Theta/\partial y|_w = 1, \quad Nu = 1/\overline{\Theta}, \tag{3.2a–c}$$

where T_∞^* is the free stream temperature, T_w^* is the wall temperature and q_w^* is the wall heat flux. Note, the bar in (3.1) and (3.2) indicates Reynolds averaging to properly define the average Nusselt number. It is apparent that for constant thermophysical properties, the Nusselt number in (3.1) and (3.2) only depends on the non-dimensional temperature Θ.

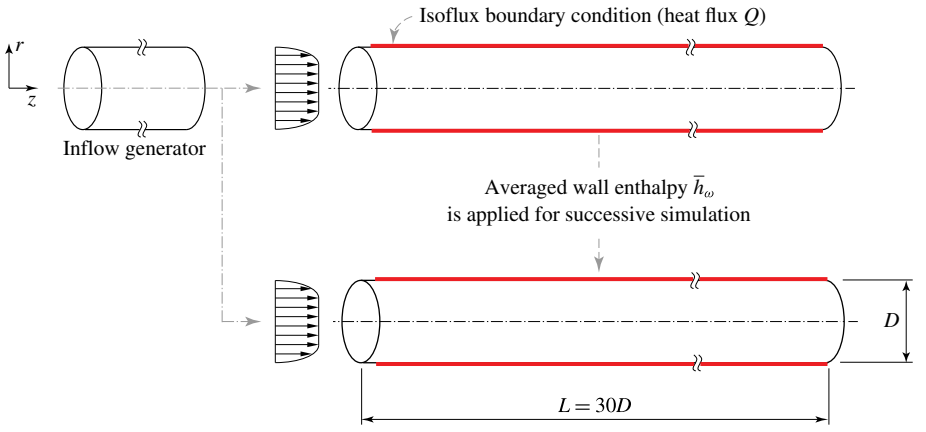

FIGURE 2. (Colour online) Simulation set-up: an inflow generator is used to provide a fully developed turbulent flow for the developing pipe flows. A simulation with constant heat flux is performed first, which then provides the averaged wall enthalpy for a successive simulation.

If the thermophysical properties are a function of temperature, the Nusselt number not only depends on the temperature but also on the thermal conductivity as follows

$$Nu = \frac{\overline{\lambda^* \dfrac{\partial T^*}{\partial y^*}}\Big|_w}{\lambda^*_{ref}(\overline{T}^*_w - T^*_b)/L^*_{ref}}. \tag{3.3}$$

Moreover, it is also not possible to use isoflux and isothermal boundary conditions and to ensure the same thermodynamic conditions at the wall.

We therefore use a different approach. First, we perform a simulation with a constant heat flux boundary condition that corresponds to a solid–fluid configuration with $K \to \infty$. The averaged wall enthalpy obtained from this simulation is then used for a successive simulation, whereby the wall enthalpy is constant in time but with the same streamwise distribution, as obtained from the simulation with the constant wall heat flux. This simulation is associated with a solid–fluid configuration with $K \to 0$. This procedure of applying a fluctuating and non-fluctuating wall temperature boundary condition is outlined in figure 2. The same approach was also performed for the constant property simulations to verify this set-up. Note, an equivalent approach would have been to first perform a simulation with an isothermal wall boundary condition ($K \to 0$), and then to use the obtained bulk enthalpy increase to calculate the streamwise heat flux distribution for the successive simulation ($K \to \infty$). Four cases have been investigated: two cases with fluid properties corresponding to supercritical CO_2 at 80 bar and two cases with a constant property fluid. For both pairs, simulations with either a fluctuating or non-fluctuating enthalpy boundary condition at the wall were performed. A summary of all case studies is given in table 1.

4. Numerical details

The numerical scheme used in this work is the same as that given in Nemati *et al.* (2015). The governing equations are solved using a staggered arrangement

Case	Fluid properties	Thermal wall boundary condition
$SC_{K\to\infty}$	Supercritical CO_2	Isoflux $Q = 2.4$
$SC_{K\to 0}$	Supercritical CO_2	Averaged wall enthalpy $\overline{h}_w$
$CP_{K\to\infty}$	Constant property	Isoflux $Q = 2.4$
$CP_{K\to 0}$	Constant property	Averaged wall enthalpy $\overline{h}_w$

TABLE 1. Case studies corresponding to thermal wall boundary conditions and fluid properties.

of the velocity components with respect to scalars in space. A second-order central difference scheme is used to discretize the spatial derivatives. The Koren slope limiter (Koren 1993) is used for the advection term in the energy equation to ensure smooth solutions in regions with sharp enthalpy gradients. The integration in time is performed similar to the method developed by Najm, Wyckoff & Knio (1998). The second-order Crank–Nicolson scheme is applied for the implicit terms (spatial derivatives in the circumferential direction in diffusive terms), and for the explicit terms the Adams–Bashforth (first sub-step) and Adams–Moulton (second sub-step) schemes are used.

The inflow conditions for the developing pipe are generated separately with a periodic adiabatic pipe flow simulation with a pipe length of $5D^*$. A no-slip boundary condition is specified for the velocity components at the wall and a convective outflow boundary condition is used for the velocities and the enthalpy. A constant heat flux of $Q = 2.4$ is imposed at the wall for the cases with a fluctuating wall temperature ($K \to \infty$) over a length of L^*. The temperature at the inlet of the pipe is set to $T_0^* = 301.15$ K, which corresponds to $h_0^* = 274.68$ kJ kg^{-1} and $Pr_0 = 3.19$ for the supercritical fluid case. The Reynolds number based on pipe diameter and friction velocity at the inlet is $Re_{\tau 0} = 360$. The conditions for the constant property cases have the same Reynolds and Prandtl number of 360 and 3.19, which are constant in space.

Several equations of state can be used to model the real gas behaviour of fluids. Currently, the most accurate equations of state in the thermodynamic region close to the critical point are multiparameter equations of state, such as the one developed by Kunz & Wagner (2012) for CO_2, as used in this work. The relations for the viscosity and thermal conductivity are given in Fenghour, Wakeham & Vesovic (1998) and Vesovic *et al.* (1990), respectively. These multiparameter equations of state and the models for the transport properties are implemented in the NIST REFPROP database (Lemmon, Huber & McLinden 2013). Because the thermodynamic pressure is constant in time and space, the density, dynamic viscosity, thermal conductivity and temperature are tabulated as a function of enthalpy and then calculated each time step using a third-order spline interpolation along the isobar of $P_0 = 80$ bar.

The mesh for the pipe for cases $SC_{K\to\infty}$ and $SC_{K\to 0}$ (see table 1) is $126 \times 288 \times 1728$ in radial, circumferential and axial directions, respectively, and has a length of $L^* = 30D^*$. For the constant property cases ($CP_{K\to\infty}$ and $CP_{K\to 0}$) a shorter pipe of $L^* = 20D^*$ and a mesh size of $126 \times 288 \times 1152$ was selected. A uniform grid spacing is used in axial and circumferential directions, while the radial grid is non-uniform and finer close to the wall. The corresponding grid resolutions are 0.55 (wall) $\leqslant \Delta r^+ \leqslant$ 4.31 (centre), $(D/2\Delta\phi)^+ = 3.93$ and $\Delta z^+ = 6.25$ in wall units based on the inlet. The thermal scales are expected to be smaller than the Kolmogorov length scale since the

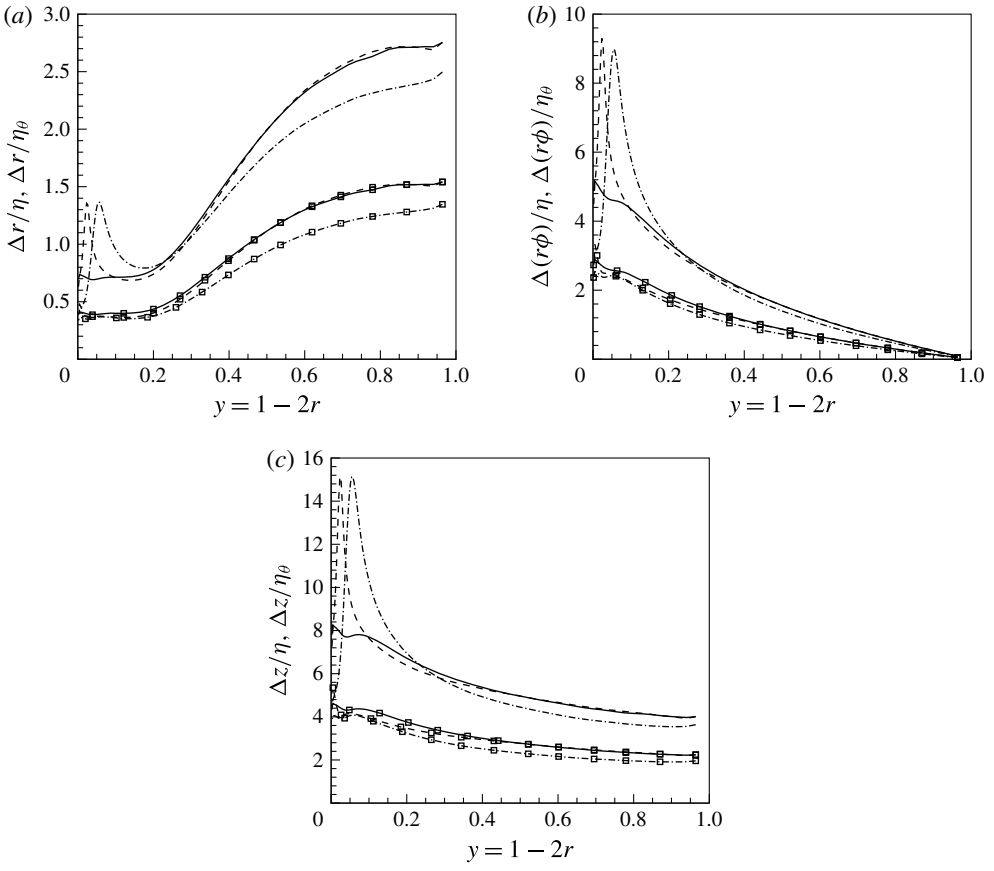

FIGURE 3. Spatial resolution normalized by Kolmogorov scale $\eta = (\overline{\nu}^3/\epsilon)^{1/4}$ (lines with symbols) and thermal scales $\eta_\theta = \eta/\sqrt{Pr}$ (lines) for $SC_{K\to\infty}$. (*a*) Radial, (*b*) circumferential and (*c*) streamwise resolution; (——) $z = 0$ ($CP_{K\to\infty}$ and $CP_{K\to 0}$), (– – –) $z = 5$, (— · —) $z = 20$.

Prandtl number $Pr > 1$. The Prandtl number at the inlet is $Pr_0 = 3.19$, whereas very close to the wall it is approximately unity. In a thin region away from the wall, where the enthalpy corresponds to the pseudo-critical value, the Prandtl number exhibits a maximum value of 14. Therefore, the radial mesh distribution has been kept constant until $y^+ \leqslant 30$ where the flow, depending on streamwise location, crosses the pseudo-critical point. For most of the remaining flow $Pr \approx 4$. Based on Tennekes & Lumley (1972), the relation between the smallest velocity scales η and the thermal structures η_θ is given as $\eta_\theta = \eta/\sqrt{Pr}$. Thus, the mesh resolution should be approximately twice – and at the location of the pseudo-critical temperature four times (see figure 1*c*) – as fine as required to resolve the velocity field. The mesh resolution in terms of the Kolmogorov η and thermal scales η_θ is shown in figure 3, where it can be seen that the Kolmogorov scales are well resolved in all directions (lines with symbols). The resolution for the thermal scales (lines) is $0.5 < \Delta y/\eta_\theta < 2.8$ in the wall-normal direction, $0.2 < \Delta(r\phi)/\eta_\theta < 9$ in the circumferential direction and $4 < \Delta x/\eta_\theta < 15$ in the streamwise direction. The local maxima of the lines correspond to the locations of the pseudo-critical point, where the spatial resolution indicates that the thermal

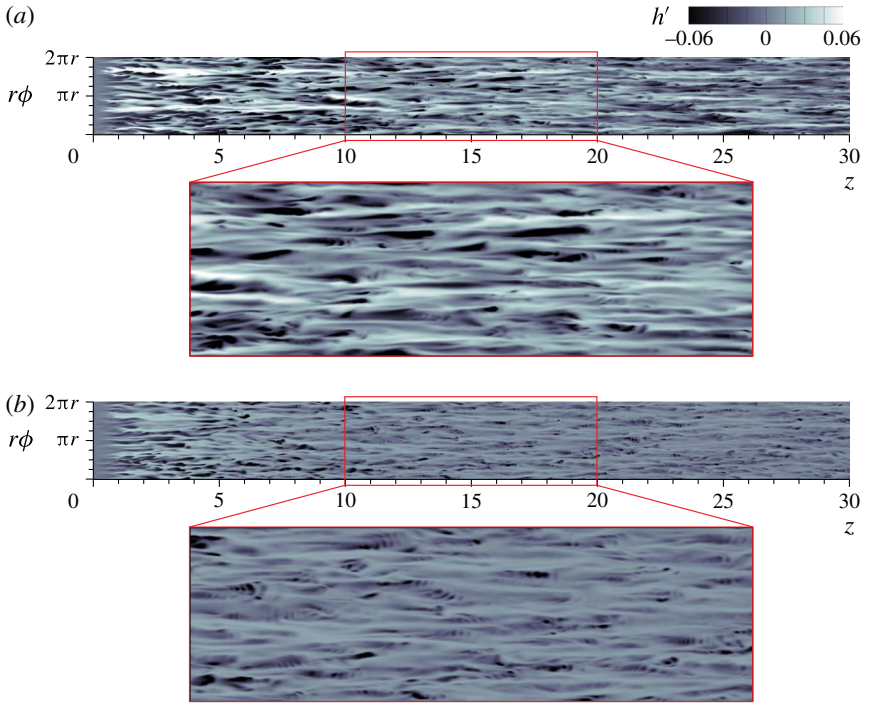

FIGURE 4. (Colour online) Instantaneous enthalpy fluctuations h' in ϕ–z at $y^+ = 2.5$ (based on inlet condition). (*a*) $\mathrm{SC}_{K\to\infty}$ and (*b*) $\mathrm{SC}_{K\to 0}$.

scales are slightly under-resolved. However, a detailed grid independency study in our previous work (Nemati *et al.* 2015) showed that the first -and second-order statistics exhibited insignificant differences for a coarser mesh with half the number of grid points in the circumferential direction. A comparable mesh resolution has been used by Zonta, Marchioli & Soldati (2012) and Lee *et al.* (2013). For example, the mesh resolution used by Lee *et al.* (2013) is $0.599 < \Delta y/\eta_\theta < 2.99$ in wall-normal direction, $\Delta z/\eta_\theta = 7.9$ in spanwise direction and $\Delta x/\eta_\theta = 12.4$ in streamwise direction.

The computer program is parallelized using the 2DECOMP&FFT library for two-dimensional pencil decomposition (Li & Laizet 2010). The simulations are performed using 1152 processors on 48 bullx B720 nodes. The time step for both inflow generator and developing pipe simulations was set to $\Delta t = 2 \times 10^{-5}$ and the corresponding maximum Courant number was 0.1. Statistics were sampled after 10 time units. The time averages were taken over 25 time units, which corresponds to 12 flow through times ($30D$). The samples were taken every 500 time steps.

5. Results and discussion

5.1. *Instantaneous fields*

The effects of the thermal wall boundary condition on turbulence can be visually highlighted by instantaneous enthalpy fluctuations in a plane parallel to the wall (ϕ–z), as depicted in figure 4. The plane is located at $y^+ = 2.5$ (based on inlet conditions), which corresponds to a wall-normal position of $y = 1 - 2r = 0.012$. It should be noted that all simulations use an identical inflow velocity field and that the enthalpy fluctuations are plotted at the same time instant.

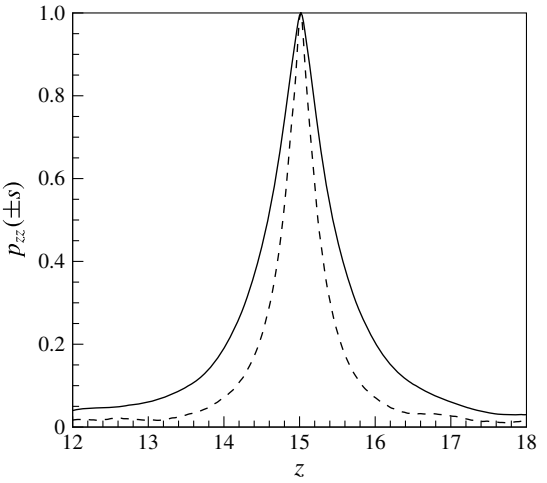

FIGURE 5. Two-point spatial correlation of enthalpy fluctuations $p_{zz}(\pm s)$ at $y^+ = 2.5$ (based on inlet condition); (——) $\mathrm{SC}_{K\to\infty}$ and (– – –) $\mathrm{SC}_{K\to 0}$.

As seen in figure 4, turbulent structures are clearly observed in enthalpy fluctuations and differences between $\mathrm{SC}_{K\to\infty}$ and $\mathrm{SC}_{K\to 0}$ are visible. The regions of low and high enthalpy fluctuations are stronger for $\mathrm{SC}_{K\to\infty}$ as compared to $\mathrm{SC}_{K\to 0}$. Similar differences in near-wall scalar fluctuations for incompressible boundary layers were reported by Kong *et al.* (2000) and Li *et al.* (2009). The plot also shows a decrease in streamwise coherency for $\mathrm{SC}_{K\to 0}$. In order to quantify the change in coherency, figure 5 shows the streamwise autocorrelation function, defined as

$$p_{zz}(\pm s) = \frac{\overline{\sqrt{\rho(r,z)}h''(r,z)\sqrt{\rho(r,z\pm s)}h''(r,z\pm s)}}{\overline{\rho(r,z)h''(r,z)h''(r,z)}} \tag{5.1}$$

at $y^+ = 2.5$ (based on inlet condition) for both $\mathrm{SC}_{K\to\infty}$ and $\mathrm{SC}_{K\to 0}$ cases. It can be seen that the autocorrelation function clearly indicates shorter structures for case $\mathrm{SC}_{K\to 0}$ as compared to $\mathrm{SC}_{K\to\infty}$. Furthermore, small-scale structures (ripples) can be observed in figure 4, which emerge after approximately $z > 10$ at the shear layers between the streaks that separate hot and cold fluid regions (see also the supplementary movie available at http://dx.doi.org/10.1017/jfm.2016.411). The strong gradients of viscosity and density across the shear layer cause destabilising effects (Govindarajan & Sahu 2014). Similar small-scale structures were also observed in Duan, Beekman & Martin (2010) for the case with strong wall cooling.

5.2. *Mean flow and turbulence statistics*

The mean quantities are obtained by taking a statistical average over time and the homogeneous circumferential direction using Reynolds and Favre averaging. Velocity components u_i and enthalpy h are Favre averaged, whereas stress tensors τ_{ij}, pressure p, heat flux q_i and thermophysical properties are Reynolds averaged. Reynolds averaging decomposes any generic variable χ into its mean $\overline{\chi}$ and its fluctuating χ' part, as $\chi = \overline{\chi} + \chi'$, with $\overline{\chi'} = 0$. For Favre averaging the generic variable is decomposed into a mean $\widetilde{\chi}$ and a fluctuating part χ'' using a density weighted average defied as $\widetilde{\chi} = \overline{\rho\chi}/\overline{\rho}$, where $\overline{\rho\chi''} = 0$.

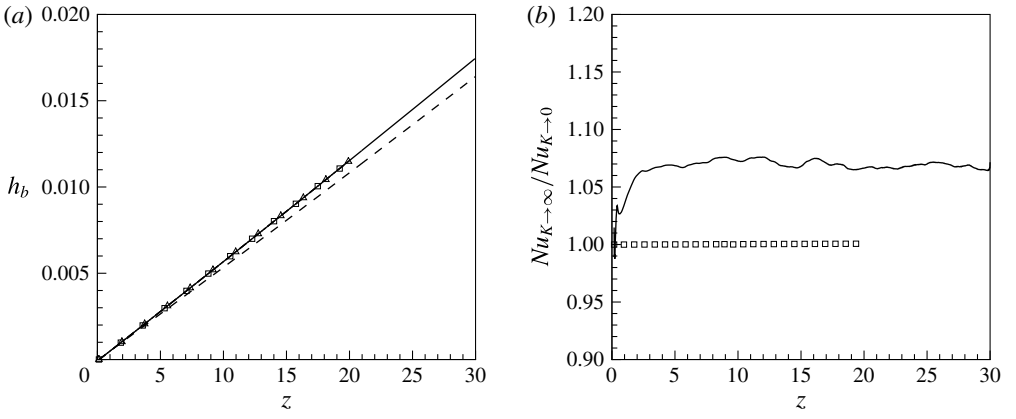

FIGURE 6. (*a*) Comparison of streamwise distributions of the bulk enthalpy h_b, (——) $\mathrm{SC}_{K\to\infty}$, (– – –) $\mathrm{SC}_{K\to0}$, (□) $\mathrm{CP}_{K\to\infty}$ and (△) $\mathrm{CP}_{K\to0}$; and (*b*) Nusselt number ratio along the pipe, (——) supercritical fluid, (□) constant property fluid.

Figure 6(*a*) shows the distribution of bulk enthalpy in the streamwise direction for all four cases. Based on the overall energy conservation, it follows that for cases with constant wall heat flux (cases $\mathrm{SC}_{K\to\infty}$ and $\mathrm{CP}_{K\to\infty}$) the distribution of the bulk enthalpy increases linearly as a function of z, namely $h_b = 4Qz/(Re_{b0}Pr_0)$. The bulk enthalpy is defined as $h_b = \int_0^R \overline{\rho u_z h} r\,\mathrm{d}r / \int_0^R \overline{\rho u_z} r\,\mathrm{d}r$. As can be seen, the symbols for the constant property cases $\mathrm{CP}_{K\to\infty}$ and $\mathrm{CP}_{K\to0}$ overlap, which highlights that the boundary condition has no influence on the global energy balance. This result agrees well with the observation from previous studies (Kays & Crawford 1993; Li *et al.* 2009) and also confirms the consistency of applying the thermal boundary conditions, as described in § 3. For the two supercritical fluid cases, however, the bulk enthalpy distributions are affected by the thermal boundary conditions. In figure 6(*a*) it can be seen that less energy is transferred to the fluid if the enthalpy at the wall is non-fluctuating ($\mathrm{SC}_{K\to0}$), and in figure 6(*b*) the Nusselt number ratio ($Nu_{K\to\infty}/Nu_{K\to0}$) shows that $Nu_{K\to\infty}$ is approximately 7 % higher for the case with the fluctuating wall enthalpy boundary condition. The Nusselt number is defined as

$$Nu = \frac{\overline{\alpha \left.\dfrac{\partial h}{\partial r}\right|_w} D}{\alpha_b(\bar{h}_w - h_b)}. \tag{5.2}$$

To investigate this Nusselt number dependency on the wall boundary condition, we will first analyse mean profiles for the enthalpy, velocity and several turbulence correlations. Figure 7 shows the radial distribution of the mean enthalpy – normalised by the value at the wall – and streamwise velocity for all cases investigated at a streamwise location of $z = 15$. Hereafter, all radial profiles are shown at $z = 15$, since this location is representative of almost the entire length of the pipe, except very close to the inlet where the heating of the pipe starts (the region between $z = 0$ and $z \approx 3$). While the constant property cases show no difference with respect to the applied boundary condition, the supercritical cases indicate a small difference. There are higher enthalpy gradients at the wall for $\mathrm{SC}_{K\to\infty}$, which support the results of a higher heat flux from the wall. The mean streamwise velocity shows only slightly

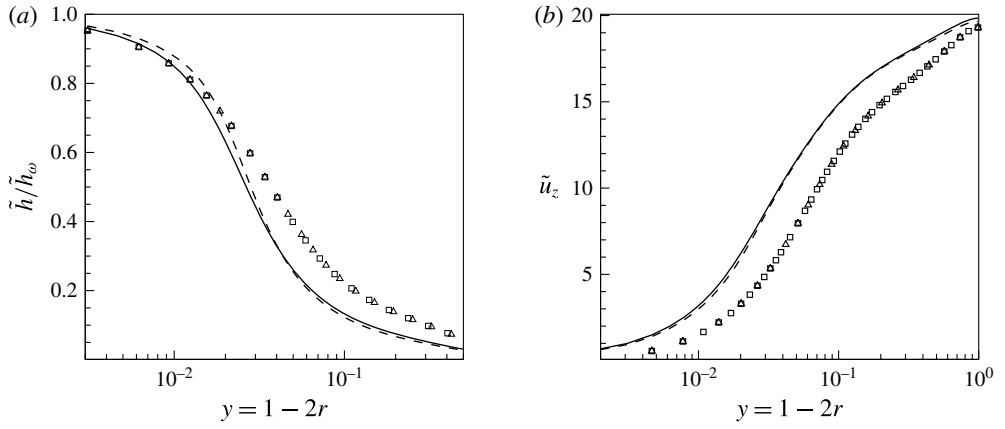

FIGURE 7. (*a*) Mean enthalpy $\tilde{h}/\tilde{h}_w$ and (*b*) streamwise velocity $\tilde{u}_z$ at $z = 15$; (——) $\mathrm{SC}_{K\to\infty}$, (– – –) $\mathrm{SC}_{K\to 0}$, (□) $\mathrm{CP}_{K\to\infty}$ and (△) $\mathrm{CP}_{K\to 0}$.

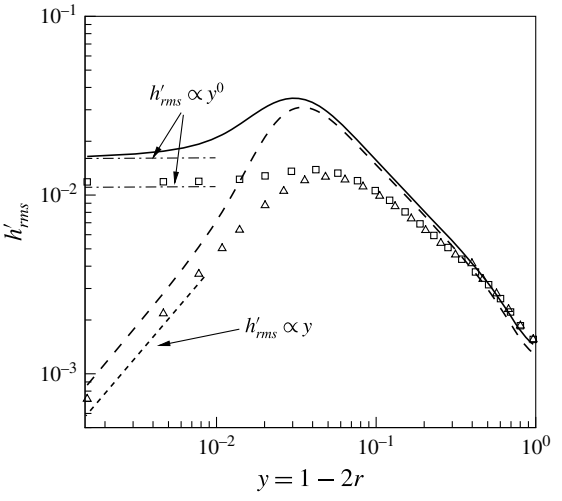

FIGURE 8. Enthalpy fluctuations h'_{rms} at $z = 15$; (——) $\mathrm{SC}_{K\to\infty}$, (– – –) $\mathrm{SC}_{K\to 0}$, (□) $\mathrm{CP}_{K\to\infty}$ and (△) $\mathrm{CP}_{K\to 0}$.

higher values for $\mathrm{SC}_{K\to\infty}$ in the near-wall region. Larger differences are obtained for the enthalpy variance h'_{rms} as shown in figure 8 for all four cases at the same streamwise location of $z = 15$. For $\mathrm{CP}_{K\to\infty}$ the variance at the wall is non-zero and its slope is zero, while for the case $\mathrm{CP}_{K\to 0}$ the value at the wall is zero and its slope is proportional to y. Similar observations were made in Kong *et al.* (2000), Tiselj *et al.* (2001*b*), Li *et al.* (2009). The supercritical cases show higher variances for both cases. However, the main difference is that for case $\mathrm{SC}_{K\to\infty}$, the slope of the enthalpy variance at the wall is non-zero. This can be explained by using Reynolds decomposition for the instantaneous heat flux:

$$\overline{\alpha}\frac{\partial \overline{h}}{\partial r}\bigg|_w + \alpha'\frac{\partial h}{\partial r}\bigg|_w + \overline{\alpha}\frac{\partial h'}{\partial r}\bigg|_w = Q \tag{5.3}$$

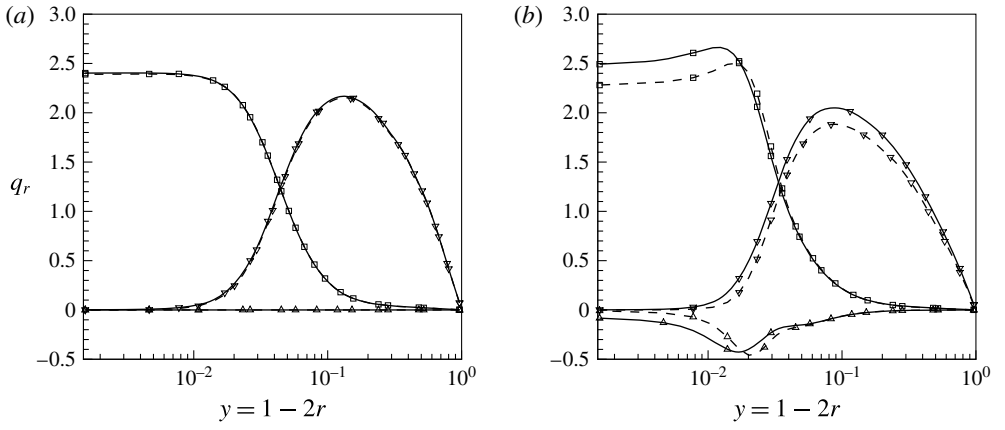

FIGURE 9. Wall-normal heat flux q_r at $z = 15$ (*a*) $\mathrm{CP}_{K\to\infty}$ and $\mathrm{CP}_{K\to 0}$ and (*b*) $\mathrm{SC}_{K\to\infty}$ and $\mathrm{SC}_{K\to 0}$; (——) $\mathrm{SC}_{K\to\infty}$ and $\mathrm{CP}_{K\to\infty}$, (– – –) $\mathrm{SC}_{K\to 0}$ and $\mathrm{CP}_{K\to 0}$, (□) $\overline{\alpha}\partial\overline{h}/\partial r$, (△) $\overline{\alpha'\partial h'/\partial r}$, (▽) $-\overline{\rho u_r'' h''} Re_{\tau 0} Pr_0$.

after multiplication with h', substituting $y = 1 - 2r$ and time averaging we obtain

$$\left.\frac{\partial \overline{h'^2}}{\partial y}\right|_w = -\left.\frac{\overline{\alpha' h' \dfrac{\partial h}{\partial y}}}{\overline{\alpha}}\right|_w . \tag{5.4}$$

Note, for the case $\mathrm{SC}_{K\to\infty}$ the wall heat flux Q is constant, and thus the term $h'Q$ vanishes after averaging. When the property fluctuations are present, as they are in case $\mathrm{SC}_{K\to\infty}$ ($\alpha' \neq 0$), the right-hand side of (5.4) does not vanish – the consequence is that the gradient of h'_{rms} at the wall is non-zero (see solid line in figure 8). The enthalpy variance for the case $\mathrm{SC}_{K\to 0}$ shows a similar behaviour as for $\mathrm{CP}_{K\to 0}$, because the fixed wall enthalpy boundary conditions results in zero and negligible property fluctuations at and close to the wall, respectively.

Next, components of the total radial heat flux are compared for different thermal wall boundary conditions. Using Reynolds decomposition, the heat flux can be decomposed as

$$q_{r,tot} = \overline{\alpha}\frac{\partial \overline{h}}{\partial r} + \overline{\alpha' \frac{\partial h'}{\partial r}} - \overline{\rho u_r'' h''} Re_{\tau 0} Pr_0, \tag{5.5}$$

where $\overline{\alpha}\partial\overline{h}/\partial r$ is the averaged molecular heat flux, $\overline{\rho u_r'' h''}$ is the turbulent heat flux and $\overline{\alpha'\partial h'/\partial r}$ is an additional averaging term due to property fluctuations. Their profiles for all cases are shown in figure 9 at $z = 15$. As can be seen in figure 9(*a*), the averaged molecular heat flux for the constant property cases is 2.4 at the wall, which corresponds to the specified heat flux value for the case $\mathrm{CP}_{K\to\infty}$; and the different thermal wall boundary conditions (cases $\mathrm{CP}_{K\to\infty}$ and $\mathrm{CP}_{K\to 0}$) have no effect on the overall heat transfer since $Pr \geqslant 1$. For the supercritical case $\mathrm{SC}_{K\to\infty}$, however, the averaged molecular heat flux at the wall is substantially higher than the specified value of 2.4 (see figure 9*b*). The additional term $\overline{\alpha'\partial h'/\partial r}$ in (5.5) causes a negative heat flux contribution of approximately -0.1. For the case $\mathrm{SC}_{K\to 0}$ the wall value

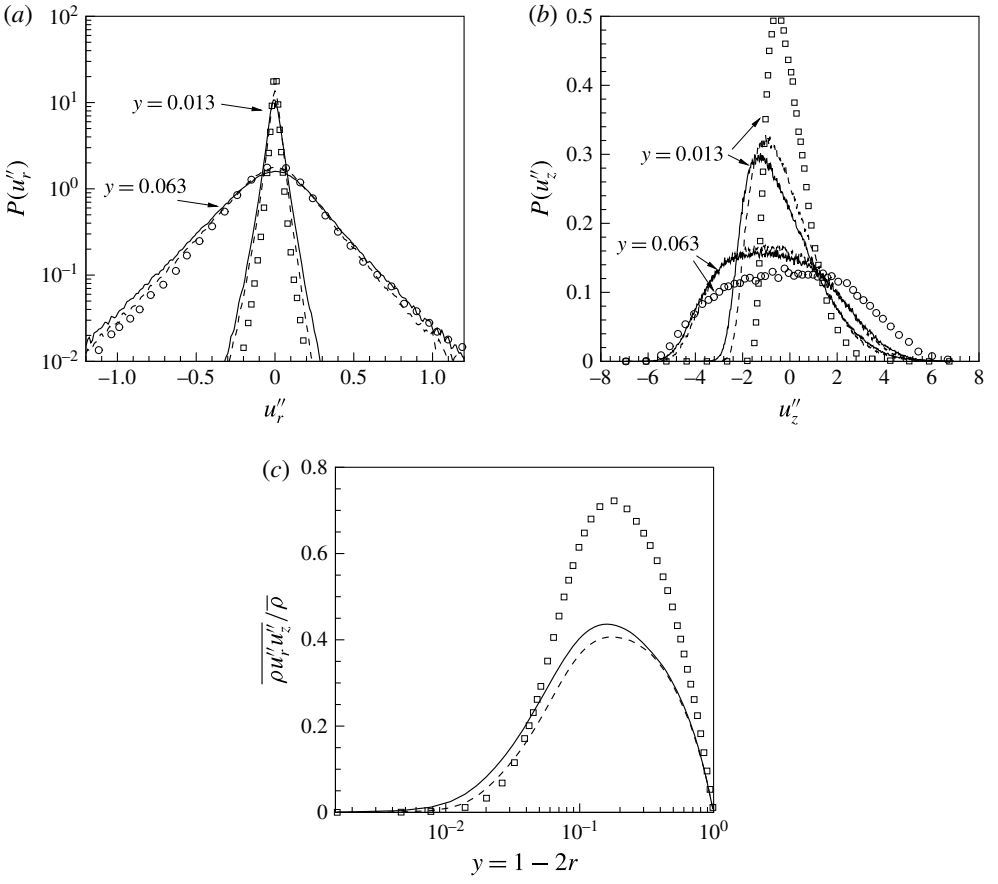

FIGURE 10. (*a*) PDF of radial velocity fluctuations u_r'', (*b*) PDF of streamwise velocity fluctuations u_z'', at two different wall-normal positions, and (*c*) turbulent shear stress profile $\overline{\rho u_r'' u_z''}$; (——) $\mathrm{SC}_{K\to\infty}$, (– – –) $\mathrm{SC}_{K\to 0}$ and symbols $\mathrm{CP}_{K\to\infty}$ ($\mathrm{CP}_{K\to 0}$) at $z = 15$.

for the averaged molecular heat flux $\overline{\alpha}\partial\overline{h}/\partial r$ is below 2.4 and the additional term $\overline{\alpha'\partial h'/\partial r} = 0$. This confirms the decreased heat transfer rate as shown in figure 6 when the constant heat flux boundary condition $\mathrm{SC}_{K\to\infty}$ is replaced by its corresponding averaged wall enthalpy in case $\mathrm{SC}_{K\to 0}$.

The effect of thermal wall boundary conditions on the averaged heat flux and the additional term is limited to the near-wall region $y \leqslant 0.03$, while the turbulent heat flux is affected over the entire cross-section of the pipe. It can be seen that $-\overline{\rho u_r'' h''}$ for $\mathrm{SC}_{K\to 0}$ is lower than for $\mathrm{SC}_{K\to\infty}$. This difference stems from the correlation between enthalpy h' and density ρ' fluctuations, whereby enhanced density fluctuations ρ' cause increased mass fluctuations and consequently larger velocity fluctuations.

This is quantified in figure 10 by means of probability density functions (PDF) of radial u_r'' and streamwise u_z'' velocity fluctuations and the turbulent shear stress. The radial u_r'' and streamwise u_z'' velocity fluctuations are compared at two different wall-normal locations for the cases $\mathrm{SC}_{K\to\infty}$ and $\mathrm{SC}_{K\to 0}$ in figures 10(*a*) and 10(*b*). Two observations can be made. First, both radial and streamwise velocity fluctuations are higher for $\mathrm{SC}_{K\to\infty}$ than for $\mathrm{SC}_{K\to 0}$ (however, more pronounced in streamwise velocity), which again can be linked to the effect of higher density fluctuations

in $SC_{K\to\infty}$. Second, the velocity fluctuations for both cases increase close to the wall, while they decrease close to the centre if compared to the $CP_{K\to 0}$ ($CP_{K\to\infty}$). The latter observation can also be seen from the profile of the Reynolds shear stress, which is plotted in figure 10(*c*) at the same streamwise position for different cases. As discussed in our previous work (Nemati *et al.* 2015), this is due to flow acceleration using thermal expansion, which results in an increase in the bulk velocity. In laminar flows, the thermal expansion increases the convective heat transfer because of flow acceleration. In turbulent convection the effects are opposite (Kim, He & Jackson 2008). Although the flow acceleration increases the velocity close to the wall, it reduces turbulence production. The wall-normal velocity gradient in the viscous dominant region increases, where it has a small influence on the turbulence production, while further away from the wall the velocity gradient decreases and thus also decreases the turbulence production.

5.3. *Quadrant analysis*

In order to identify the fractional contributions of instantaneous fluctuations to turbulence statistics, such as the turbulent heat flux $\overline{\rho u_r'' h''}$ and the turbulent shear stress $\overline{\rho u_r'' u_z''}$, a quadrant analysis is performed next. For this technique, $\overline{\rho u_r'' h''}$ and $\overline{\rho u_r'' u_z''}$ are conditionally averaged into four quadrants of $\sqrt{\rho}u_r'' - \sqrt{\rho}h''$ and $\sqrt{\rho}u_r'' - \sqrt{\rho}u_z''$ planes, respectively, as shown in figure 11. The first quadrant $Q1$ is associated with sweep events since cold and high-speed fluid moves toward the wall and the third quadrant $Q3$ indicates ejections, which are hot fluids with low streamwise velocity moving away from the wall. The second quadrant $Q2$ contains outward motions of high-speed and cold fluids, while the fourth quadrant $Q4$ contains events of inward motions with low-speed hot fluids. Figure 11(*a*) shows the contributions from each quadrant to the radial turbulent heat flux $\overline{\rho u_r'' h''}$ plotted as a function of wall-normal coordinate. In the case of non-fluctuating wall temperature (case $SC_{K\to 0}$), all contributions to the turbulent heat flux are attenuated. It can be seen that the $Q1$ and $Q3$ events, which have the largest contributions, are smaller for case $SC_{K\to 0}$ than for $SC_{K\to\infty}$. In other words, for the case $SC_{K\to 0}$ the hot fluid has less tendency to leave the wall, which consequently leads to the lower heat transfer.

The fractional contributions to the Reynolds shear stress $\overline{\rho u_r'' u_z''}$ are shown in figure 11(*b*) for $SC_{K\to\infty}$ and $SC_{K\to 0}$. Similar to the turbulent heat flux, all contributions to the Reynolds shear stress are decreased when the fluctuating wall temperature ($SC_{K\to\infty}$) is changed to the non-fluctuating wall temperature condition ($SC_{K\to 0}$). Sweep $Q1$ and ejection $Q3$ events, which have positive contributions to the Reynolds shear stress, show the largest differences. Choi, Moin & Kim (1994) reported that reduction in $Q1$ and $Q3$ events result in skin friction reduction.

5.4. *Turbulence budgets*

To study the effect of different enthalpy wall boundary conditions on the averaged transport equation for turbulence kinetic energy and wall-normal turbulent heat flux, their budgets are examined next. The evolution equation for the Favre-averaged turbulence kinetic energy is $k = 1/2\widetilde{u_i'' u_i''}$ can be written as follows (Huang, Coleman & Bradshaw 1995):

$$\frac{\partial \overline{\rho} k}{\partial t} + C_k = P_k + T_k + \Pi_k + \Phi_k + V_k + \epsilon_k + E_k^{(1)} + E_k^{(2)}, \tag{5.6}$$

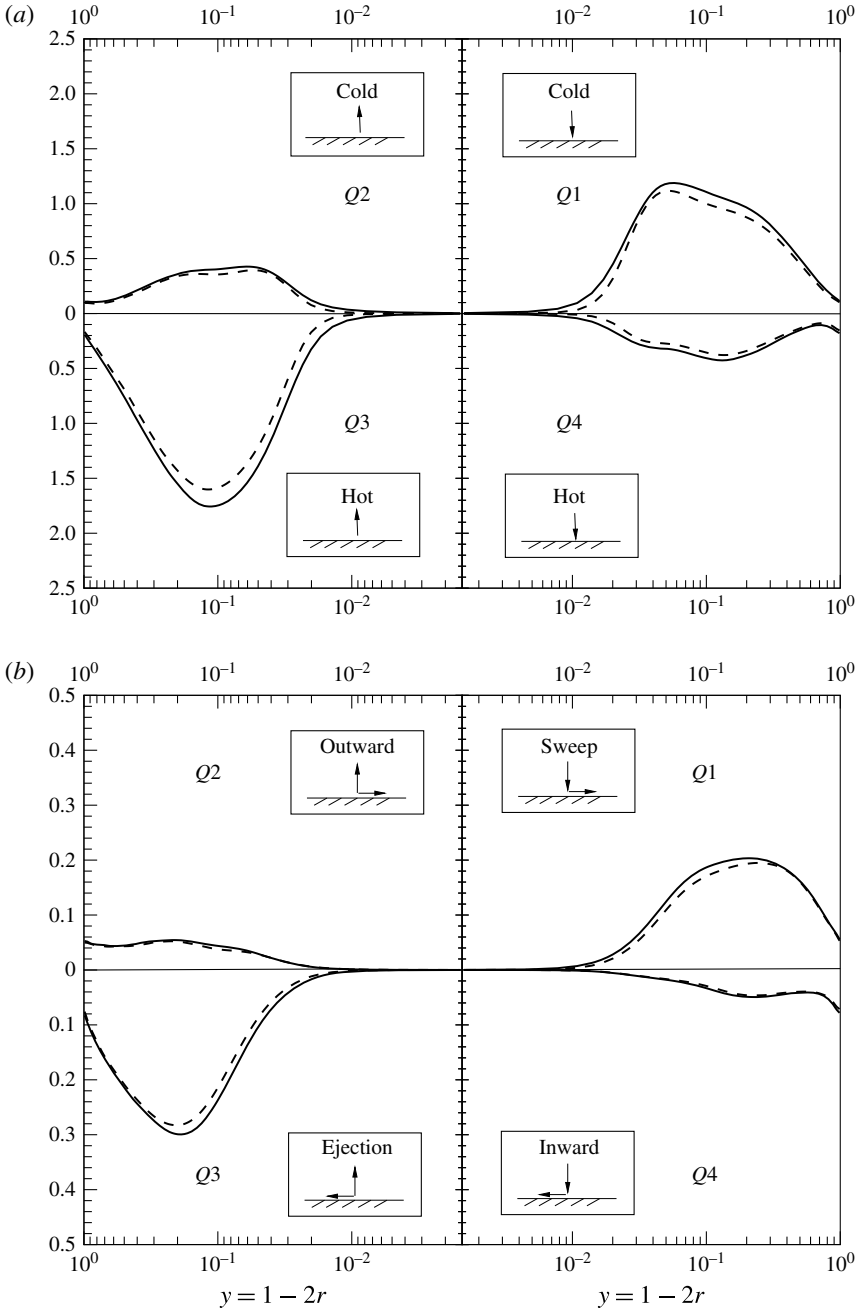

FIGURE 11. Fractional contribution to the (*a*) radial turbulent heat flux $\overline{\rho u_r'' h''}$ and (*b*) Reynolds shear stress $\overline{\rho u_r'' u_z''}$ at $z = 15$; (——) $\mathrm{SC}_{K\to\infty}$, (– – –) $\mathrm{SC}_{K\to 0}$.

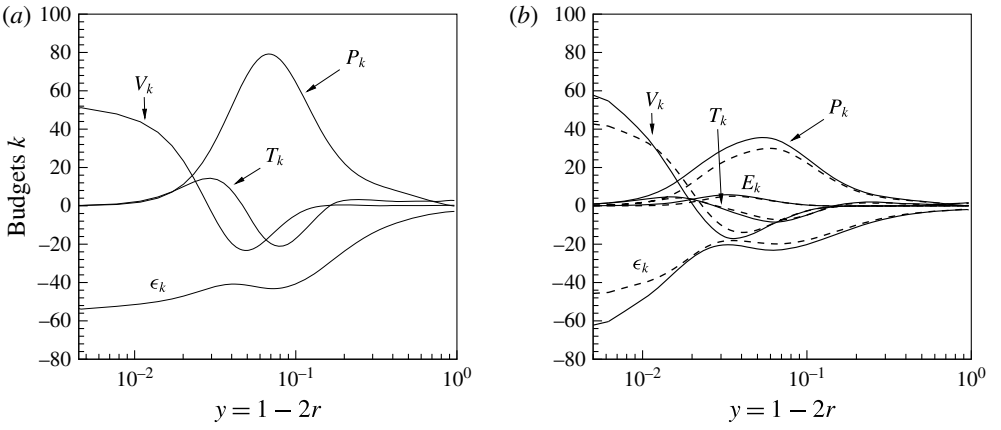

FIGURE 12. Turbulence kinetic energy $k = 1/2\widetilde{u_i''u_i''}$ budgets at $z = 15$ (*a*) $\mathrm{CP}_{K\to\infty}$ ($\mathrm{CP}_{K\to 0}$), (*b*) (——) $\mathrm{SC}_{K\to\infty}$ and (– – –) $\mathrm{SC}_{K\to 0}$. Note, the profiles for $\mathrm{CP}_{K\to\infty}$ ($\mathrm{CP}_{K\to 0}$) are equivalent to $z = 0$ for the SC cases.

with

$$\left.\begin{aligned} C_k &= \frac{\partial \overline{\rho}\tilde{u}_j k}{\partial x_j}, \quad P_k = -\overline{\rho u_i'' u_j''}\frac{\partial \tilde{u}_j}{\partial x_i}, \quad T_k = -\frac{1}{2}\frac{\partial \overline{\rho u_i'' u_i'' u_j''}}{\partial x_j}, \\ \Pi_k &= -\frac{\partial \overline{p' u_j''}}{\partial x_j}, \quad \Phi_k = \overline{p'\frac{\partial u_j''}{\partial x_j}}, \quad V_k = \frac{1}{Re_{\tau 0}}\frac{\partial \overline{\tau_{ij}' u_i''}}{\partial x_j}, \\ \epsilon_k &= -\frac{1}{Re_{\tau 0}}\overline{\tau_{ij}'\frac{\partial u_i''}{\partial x_j}}, \quad E_k^{(1)} = \overline{u_i''}\frac{1}{Re_{\tau 0}}\frac{\partial \overline{\tau}_{ij}}{\partial x_j}, \quad E_k^{(2)} = -\overline{u_i''}\frac{\partial \overline{p}}{\partial x_i}, \end{aligned}\right\} \tag{5.7}$$

where

$$\overline{\tau}_{ij} = \overline{\mu}\left(\frac{\partial \overline{u}_i}{\partial x_j} + \frac{\partial \overline{u}_j}{\partial x_i}\right) + \overline{\mu'\left(\frac{\partial u_i'}{\partial x_j} + \frac{\partial u_j'}{\partial x_i}\right)} - \frac{2}{3}\overline{\mu}\frac{\partial \overline{u_k}}{\partial x_k}\delta_{ij} - \frac{2}{3}\overline{\mu'\frac{\partial u_k'}{\partial x_k}}\delta_{ij}, \quad \tau_{ij}' = \tau_{ij} - \overline{\tau}_{ij}. \tag{5.8a,b}$$

The terms in (5.7) are mean convection C_k, turbulence production P_k, turbulence diffusion T_k, pressure diffusion Π_k, pressure dilatation Φ_k, viscous diffusion of turbulence kinetic energy V_k, turbulence dissipation ϵ_k and $E_k^{(l)}(l = 1, 2)$ are additional terms due to density and velocity fluctuations. These terms are referred to as additional correlations and result from turbulent fluctuations that are responsible for energy exchange between mean and turbulence kinetic energy (see Huang *et al.* 1995). Emphasis is given to P_k, T_k, V_k, ϵ_k and $E_k = \sum_{l=1}^{2} E_k^{(l)}$ and their profiles are shown in figure 12 for all cases at $z = 15$. Note, the budgets for the constant property cases shown in figure 12(*a*) do not change in the streamwise direction, since the energy equation is a passive scalar and the velocity field is unaffected by the heat transfer. Thus, the profiles in figure 12(*a*) also correspond to the inlet condition for the supercritical cases as shown in figure 12(*b*).

As discussed in our previous work (Nemati *et al.* 2015), flow acceleration due to thermal expansion causes a decrease in turbulence for the supercritical cases. The production rate in figure 12(*b*) is substantially lower than for the constant property case in figure 12(*a*). The turbulence dissipation also shows a reduction for both

supercritical cases, except for $\mathrm{SC}_{K\to\infty}$ very close to the wall. An equivalent effect has been observed in Zonta *et al.* (2012), where they studied the effect of viscosity variations on turbulence statistics in fully developed channel flows. They observed that on the hot side of the channel (low viscosity) the turbulent dissipation decreases above the viscous sublayer, but increases between the viscous sublayer and the wall. The turbulent diffusion T_k is reduced due to the reduction in turbulence caused by flow acceleration and thermal expansion.

With respect to the different boundary conditions, it can be seen that the turbulence production P_k experiences a larger reduction for the non-fluctuating wall enthalpy case $\mathrm{SC}_{K\to 0}$ as compared to $\mathrm{SC}_{K\to\infty}$. This can be further analysed by expanding P_k, in cylindrical coordinates, to

$$P_k = -\overline{\rho u_r'' u_r''}\frac{\partial \tilde{u}_r}{\partial r} - \overline{\rho u_r'' u_z''}\frac{\partial \tilde{u}_r}{\partial z} - \overline{\rho u_\phi'' u_\phi''}\frac{\tilde{u}_r}{r} - \overline{\rho u_r'' u_z''}\frac{\partial \tilde{u}_z}{\partial r} - \overline{\rho u_z'' u_z''}\frac{\partial \tilde{u}_z}{\partial z}. \tag{5.9}$$

The product of Reynolds shear stress and streamwise velocity gradient is the dominant source of turbulence kinetic energy production (fourth term in (5.9)). Based on the results discussed in § 5.2, the higher P_k in $\mathrm{SC}_{K\to\infty}$ can thus be explained by the higher Reynolds shear stress $\overline{\rho u_r'' u_z''}$ (figure 10*c*), since the streamwise velocity gradient shows only small differences in the near-wall region (figure 7*b*). The turbulence dissipation in $\mathrm{SC}_{K\to 0}$ is slightly smaller over the entire cross-section of the pipe, than it is for $\mathrm{SC}_{K\to\infty}$, but larger differences are observed very close to the wall. This is a direct consequence of the higher gradients in velocity fluctuations for case $\mathrm{SC}_{K\to\infty}$. The larger dissipation in the near-wall region is balanced with a higher energy transfer due to viscous diffusion in the near-wall region for case $\mathrm{SC}_{K\to\infty}$. The turbulence diffusion T_k, and the additional terms are less affected by the thermal boundary condition. As can be seen, the additional terms $E_k^{(1)}$ and $E_k^{(2)}$ contribute to the production and sink of turbulence kinetic energy, respectively. Figure 13 shows the largest components of $E_k^{(1)}$ and $E_k^{(2)}$ at $z = 15$ for $\mathrm{SC}_{K\to\infty}$ and $\mathrm{SC}_{K\to 0}$. The term $\overline{u_z''}(\partial r\overline{\tau}_{rz}/r\partial r)/Re_{\tau 0}$ (part of $E_k^{(1)}$) corresponds to a source (energy is received from the mean flow), whereas the term $-\overline{u_z''}\partial\overline{p}/\partial z$ (part of $E_k^{(2)}$) corresponds to a sink (energy is transferred to the mean flow) of turbulent kinetic energy. Comparing these two additional terms for the cases $\mathrm{SC}_{K\to\infty}$ and $\mathrm{SC}_{K\to 0}$, it is possible to observe a reduction in magnitude for $\mathrm{SC}_{K\to 0}$ that stems from the difference in streamwise velocity fluctuations (see figure 10*b*) in the near-wall region.

Similar to the turbulence kinetic energy, an evolution equation for the Favre-averaged turbulent heat flux can be formulated as:

$$\frac{\partial\overline{\rho u_i'' h''}}{\partial t} + C_{e,i} = P_{e,i} + T_{e,i} + \Pi_{e,i} + V_{e,i} + \epsilon_{e,i} + E_{e,i}, \tag{5.10}$$

with

$$\left.\begin{aligned} C_{e,i} &= \frac{\partial \tilde{u}_j \overline{\rho u_i'' h''}}{\partial x_j}, \quad P_{e,i} = -\overline{\rho u_j'' h''}\frac{\partial \tilde{u}_i}{\partial x_j} - \overline{\rho u_i'' u_j''}\frac{\partial \tilde{h}}{\partial x_j}, \quad T_{e,i} = -\frac{\partial \overline{\rho u_i'' u_j'' h''}}{\partial x_j}, \\ \Psi_{e,i} &= -\overline{h''\frac{\partial p'}{\partial x_i}}, \quad V_{e,i} = \frac{1}{Re_{\tau 0}}\frac{\partial \overline{\tau_{ij}' h''}}{\partial x_j} + \frac{1}{Re_{\tau 0}Pr_0}\frac{\partial \overline{q_j' u_i''}}{\partial x_j}, \\ \epsilon_{e,i} &= -\frac{1}{Re_{\tau 0}}\overline{\tau_{ij}'\frac{\partial h''}{\partial x_j}} - \frac{1}{Re_{\tau 0}Pr_0}\overline{q_j'\frac{\partial u_i''}{\partial x_j}}, \\ E_{e,i}^{(1)} &= \overline{h''}\left(\frac{1}{Re_{\tau 0}}\frac{\partial \overline{\tau}_{ij}}{\partial x_j} - \frac{\partial \overline{p}}{\partial x_i}\right), \quad E_{e,i}^{(2)} = \frac{1}{Re_{\tau 0}Pr_0}\overline{u_i''}\frac{\partial \overline{q}_j}{\partial x_j}, \end{aligned}\right\} \tag{5.11}$$

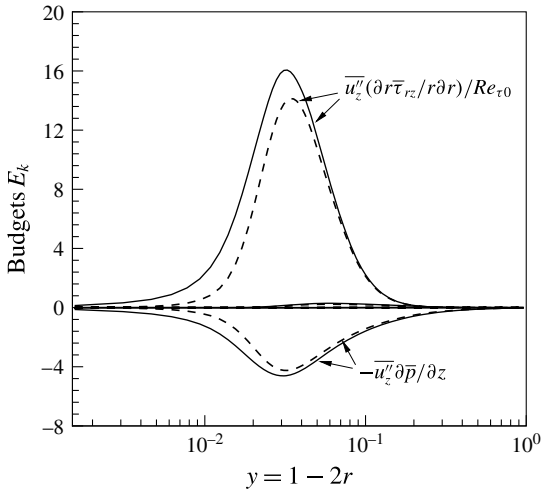

FIGURE 13. Largest components of $E_k^{(1)}$ and $E_k^{(2)}$; (——) $\mathrm{SC}_{K\to\infty}$, (– – –) $\mathrm{SC}_{K\to 0}$.

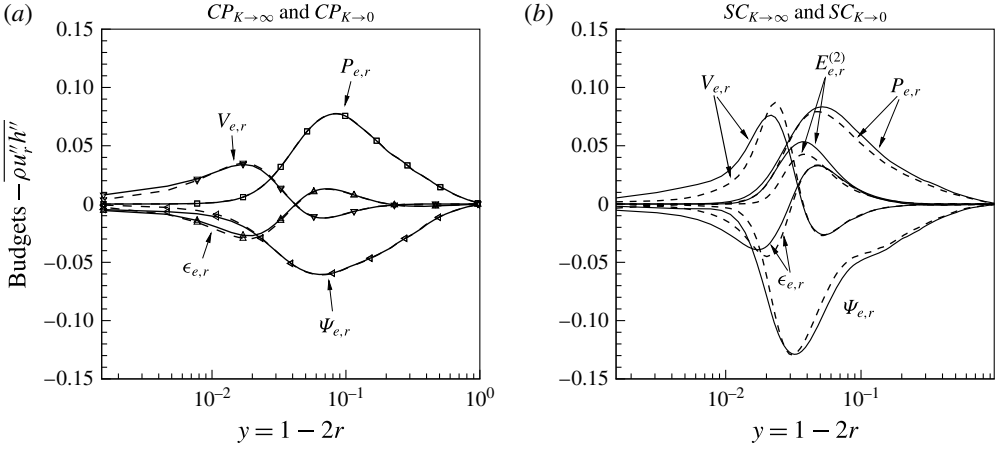

FIGURE 14. Wall-normal turbulent heat flux $-\overline{\rho u_r'' h''}$ budgets at $z = 15$, (——) $\mathrm{SC}_{K\to\infty}$ and $\mathrm{CP}_{K\to\infty}$, (– – –) $\mathrm{SC}_{K\to 0}$ and $\mathrm{CP}_{K\to 0}$.

where

$$\overline{q}_i = -\overline{\alpha}\frac{\partial \overline{h}}{\partial x_j} - \overline{\alpha' \frac{\partial h'}{\partial x_j}}, \quad q_i' = q_i - \overline{q}_i. \tag{5.12a,b}$$

Here the terms are mean convection $C_{e,i}$, production $P_{e,i}$, turbulence diffusion $T_{e,i}$, enthalpy–pressure-gradient correlation $\Psi_{e,i}$, molecular diffusion $V_{e,i}$, dissipation of turbulent heat flux $\epsilon_{e,i}$ and $E_{e,i}^{(l)} (l = 1, 2)$ are additional terms that stem from density, velocity and enthalpy fluctuations. Figure 14 shows profiles of $P_{e,r}$, $\Psi_{e,r}$, $V_{e,r}$, $\epsilon_{e,r}$ and $E_{e,r}^{(2)}$ (remaining terms are insignificant) for the constant property and the supercritical pressure cases with different wall enthalpy boundary conditions at $z = 15$. It is evident from figure 14(*a*) that the budgets for the constant property cases with different boundary conditions collapse over a wide range. Only minor differences

between $\mathrm{CP}_{K\to\infty}$ and $\mathrm{CP}_{K\to 0}$ appear for the dissipation $\epsilon_{e,r}$, viscous diffusion $V_{e,r}$ and enthalpy–pressure-gradient correlation $\Psi_{e,r}$ very close to the wall. This is due to the wall enthalpy fluctuations in case $\mathrm{CP}_{K\to\infty}$. The production $P_{e,r}$ does not change, because it contains products of turbulent heat flux and velocity gradients, and turbulent stresses and enthalpy gradients, see (5.11). Because none of these terms change (see figures 7*a* and 9*a*) with respect to thermal boundary conditions, also $P_{e,r}$ is unaffected. The terms $\epsilon_{e,r}$, $V_{e,r}$ and $\Psi_{e,r}$ contain products of h'' with velocity and pressure gradients. Because, h'' is affected by the thermal boundary conditions, also $\epsilon_{e,r}$, $V_{e,r}$ and $\Psi_{e,r}$ change.

If the constant property and the supercritical fluid cases are compared, it can be seen that, although the production $P_{e,r}$ of the turbulent heat flux are nearly the same for both fluids, the main destruction $\Psi_{e,r}$ substantially differs. For the supercritical fluid cases $\mathrm{SC}_{K\to\infty}$ and $\mathrm{SC}_{K\to 0}$ the enthalpy–pressure-gradient correlation $\Psi_{e,r}$ is mainly balanced by $P_{e,r}$ and the additional term $E^{(2)}_{e,r}$, which is a source of turbulent heat flux that only appears for the supercritical fluid cases. Unlike for the constant property cases shown in figure 14(*a*), the effect of thermal wall boundary conditions on the turbulent heat flux budgets is larger for the variable property cases in figure 14(*b*). Similar to the turbulence kinetic energy budgets, the production for case $\mathrm{SC}_{K\to\infty}$ is larger than for $\mathrm{SC}_{K\to 0}$. The enthalpy–pressure-gradient correlation $\Psi_{e,r}$ shows larger values for $\mathrm{SC}_{K\to\infty}$ than for $\mathrm{SC}_{K\to 0}$ case. The decreased enthalpy–pressure-gradient correlation for $\mathrm{SC}_{K\to 0}$ is mainly because of the decreased enthalpy fluctuation, while the gradient of the pressure fluctuations does not show major differences (not shown here). The additional term $E^{(2)}_{e,r}$, the dissipation $\epsilon_{e,r}$ and the viscous diffusion $V_{e,r}$ show larger values in the near-wall region for case $\mathrm{SC}_{K\to\infty}$, which is due to the higher velocity and enthalpy fluctuations.

5.5. *Decomposition of skin friction coefficient and Nusselt number*

To quantify the individual laminar and turbulent contributions to the total skin friction and heat transfer we derive and apply the Fukagata, Iwamoto & Kasagi (FIK) identity for the heated pipe that contains the fluid at supercritical pressure. The FIK identity was derived by Fukagata *et al.* (2002) to investigate componential contributions that different dynamical effects have on global integral quantities. Since then it has been used extensively to study drag reduction mechanisms and active control strategies in fully developed channel and pipe flows (Fukagata & Kasagi 2003), developing turbulent boundary layers with suction and blowing (Kametani & Fukagata 2011), heated developing turbulent boundary layers (Lee *et al.* 2013) and compressible flows (Gomez, Flutet & Sagaut 2009). Fukagata, Iwamoto & Kasagi (2005) also used the same approach to derive an identity relation for the Nusselt number and turbulent heat flux in fully developed incompressible channel flows.

In this work we re-derive the FIK identity to take into account the strong property fluctuations in supercritical fluids, by integrating the streamwise momentum and enthalpy equations twice in the radial direction. The FIK identity for the skin friction reads:

$$C_{f,FIK} = \underbrace{-\frac{2}{\rho_b U_b^2 Re_{\tau 0}}\int_0^R r\overline{\mu}\overline{S}_{rz} r\,\mathrm{d}r}_{C_I} + \underbrace{\frac{2}{\rho_b U_b^2}\int_0^R r\overline{\rho u_r'' u_z''} r\,\mathrm{d}r}_{C_{II}} + \underbrace{\frac{1}{\rho_b U_b^2}\int_0^R (R^2 - r^2)\left\langle\frac{\partial \overline{p}}{\partial z}\right\rangle r\,\mathrm{d}r}_{C_{III}}$$

$$+\underbrace{\frac{1}{\rho_b U_b^2}\int_0^R r\overline{\rho}\tilde{u}_r\tilde{u}_z r\,\mathrm{d}r}_{C_{IV}}+\underbrace{\frac{1}{\rho_b U_b^2}\int_0^R (R^2-r^2)\left\langle\frac{\partial\overline{\rho}\tilde{u}_z\tilde{u}_z}{\partial z}\right\rangle r\,\mathrm{d}r}_{C_V}$$
$$+\underbrace{\frac{1}{\rho_b U_b^2}\int_0^R (R^2-r^2)\left\langle\frac{\partial\overline{\rho u_z'' u_z''}}{\partial z}\right\rangle r\,\mathrm{d}r}_{C_{VI}}$$
$$\underbrace{-\frac{1}{\rho_b U_b^2 Re_{\tau 0}}\int_0^R (R^2-r^2)\left\langle\frac{1}{r}\frac{\partial r\overline{\mu' S'}_{rz}}{\partial r}\right\rangle r\,\mathrm{d}r}_{C_{VII}}$$
$$\underbrace{-\frac{1}{\rho_b U_b^2 Re_{\tau 0}}\int_0^R (R^2-r^2)\left\langle\frac{\partial\overline{\mu}\overline{S}_{zz}}{\partial z}\right\rangle r\,\mathrm{d}r}_{C_{VIII}}$$
$$\underbrace{-\frac{1}{\rho_b U_b^2 Re_{\tau 0}}\int_0^R (R^2-r^2)\left\langle\frac{\partial\overline{\mu' S'}_{zz}}{\partial z}\right\rangle r\,\mathrm{d}r}_{C_{IX}}, \tag{5.13}$$

where $\langle\ \rangle$ indicates the following operation

$$\langle\Phi(r,z)\rangle=\Phi(r,z)-\frac{2}{R^2}\int_0^R\Phi(r,z)r\,\mathrm{d}r. \tag{5.14}$$

Equation (5.13) shows that the skin friction coefficient can be decomposed into a laminar contribution C_I, which for a constant property fluid is identical to the analytical solution for laminar flows $16/Re_{b0}$, a turbulent contribution C_{II} and several inhomogeneous contributions C_{II}–C_{IX}. The merit of this equation is that different contributions to skin friction can be compared for fluids with constant or variable properties.

The results of (5.13) are plotted in figure 15 (note, insignificant terms are not shown). In order to verify the FIK derivation, the sum of all terms is compared first with the locally calculated wall shear stress $C_f=2\tau_w/(\rho_b U_b^2)$ for $\mathrm{CP}_{K\to\infty}$, $\mathrm{SC}_{K\to\infty}$ and $\mathrm{SC}_{K\to 0}$. An excellent agreement is obtained ensuring correctness and consistency (symbols and line overlap). As expected, for $\mathrm{CP}_{K\to\infty}$ (results for $\mathrm{CP}_{K\to 0}$ are identical and thus not shown) the laminar and turbulent contributions are $0.00302=16/Re_{b0}$ and 0.00620, respectively. These contributions are identical to the results of a fully developed pipe flow that have also been reported by Fukagata *et al.* (2002).

Unlike for the constant property cases, the inhomogeneous contributions play a significant role for the skin friction in the supercritical cases (see figure 15*b*). The term related to the streamwise momentum flux C_V is negative at the inlet and becomes positive at $z\approx 7$. At the beginning of the pipe, the thermal boundary layer is very thin. The density rapidly decreases close to the wall and the mass flux increases. To satisfy the mass flux balance, the velocity in the core region decreases, which also causes a decrease of momentum flux $\overline{\rho}\tilde{u}_z\tilde{u}_z$. Proceeding downstream, the thermal boundary layer grows until a net positive value of C_V is reached at $z\approx 7$ (note, the weighting factor $r(R^2-r^2)$ within the integral is zero at the wall and R^2 at the cell centre). In contrast to C_V, the magnitude of the term C_{IV} (the product of the mean density, mean wall-normal and streamwise velocities) experiences a sharp

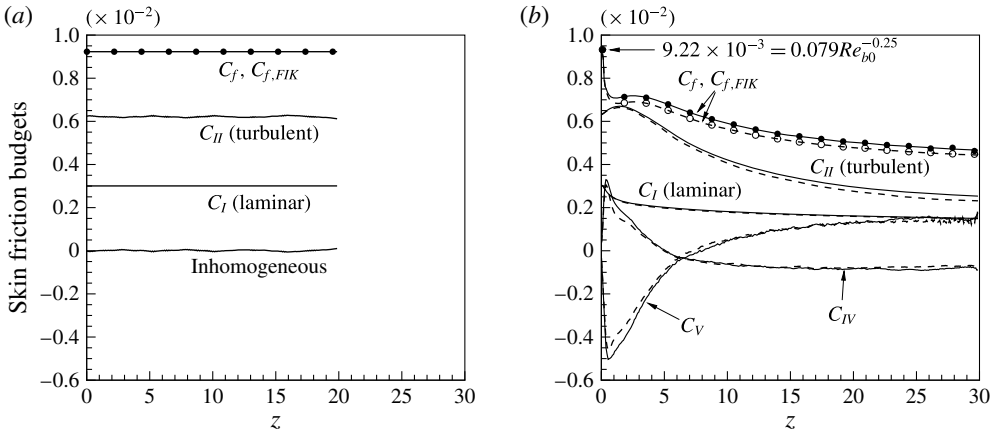

FIGURE 15. Componential contributions to the skin friction. The lines indicate the individual terms as given in (5.13) and the symbols indicate the locally computed skin friction C_f, (*a*) (——) $\mathrm{CP}_{K\to\infty}$, (– – –) $\mathrm{CP}_{K\to 0}$; (*b*) (——) $\mathrm{SC}_{K\to\infty}$, (– – –) $\mathrm{SC}_{K\to 0}$.

increase in the inlet region and shows a peak value of 0.33 at $z = 0.7$. Afterwards C_{IV} decreases and reaches a negative value of -0.09 at $z = 17$. This can be explained by the sharp changes of streamwise velocity in the near-wall region, which results in a high positive wall-normal velocity close to the inlet and negative wall-normal velocity further downstream. The contributions of C_I (laminar) and C_{II} (turbulent) to the skin friction show a decreasing trend, due to the reduction in mean viscosity and Reynolds shear stress, respectively.

Figure 15(*b*) shows that the skin friction for $\mathrm{SC}_{K\to\infty}$ is higher along the pipe than for $\mathrm{SC}_{K\to 0}$. Comparing the individual contributions for $\mathrm{SC}_{K\to\infty}$ and $\mathrm{SC}_{K\to 0}$, it can be seen that the major difference in $C_{f,FIK}$ stems from the turbulent contribution C_{II}.

As explained in § 5.3, the lower values of C_{II} for $\mathrm{SC}_{K\to 0}$ are due to the lower Reynolds shear stress, as also shown in figure 11(*b*). In conclusion, the non-fluctuating wall enthalpy boundary condition causes the skin friction for case $\mathrm{SC}_{K\to 0}$ to reduce by approximately 6 %.

Similar to the skin friction, the FIK identity for the Nusselt number reads:

$$Nu_{FIK} = \underbrace{\frac{32}{\alpha_b(\overline{h}_w - h_b)}\int_0^R r\overline{\alpha}\frac{\partial \overline{h}}{\partial r}r\,\mathrm{d}r}_{H_I} \underbrace{-\frac{32Re_{\tau 0}Pr_0}{\alpha_b(\overline{h}_w - h_b)}\int_0^R r\overline{\rho h'' u_r''}r\,\mathrm{d}r}_{H_{II}}$$
$$\underbrace{-\frac{16Re_{\tau 0}Pr_0}{\alpha_b(\overline{h}_w - h_b)}\int_0^R (R^2 - r^2)\left\langle \frac{1}{r}\frac{\partial r\overline{\rho}\tilde{h}\tilde{u}_r}{\partial r}\right\rangle r\,\mathrm{d}r}_{H_{III}}$$
$$\underbrace{-\frac{16Re_{\tau 0}Pr_0}{\alpha_b(\overline{h}_w - h_b)}\int_0^R (R^2 - r^2)\left\langle \frac{\partial \overline{\rho}\tilde{h}\tilde{u}_z}{\partial z}\right\rangle r\,\mathrm{d}r}_{H_{IV}}$$

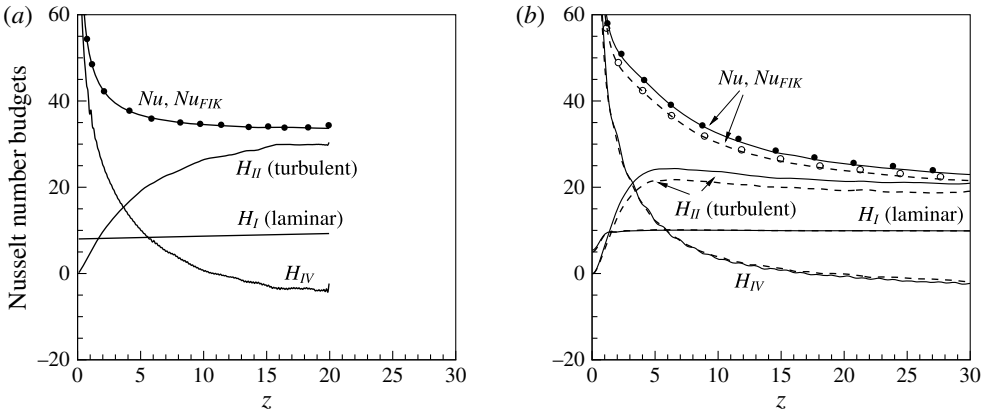

FIGURE 16. Componential contributions to the Nusselt number. The lines indicate the individual terms in (5.15) and the symbols indicate the locally computed Nusselt number Nu, (*a*) (——) $\mathrm{CP}_{K\to\infty}$; (*b*) (——) $\mathrm{SC}_{K\to\infty}$, (– – –) $\mathrm{SC}_{K\to 0}$.

$$
\begin{aligned}
&\underbrace{-\frac{16Re_{\tau 0}Pr_0}{\alpha_b(\bar{h}_w-h_b)}\int_0^R (R^2-r^2)\left\langle\frac{\partial\overline{\rho h'' u_z''}}{\partial z}\right\rangle r\,\mathrm{d}r}_{H_V}\\
&+\underbrace{\frac{16}{\alpha_b(\bar{h}_w-h_b)}\int_0^R (R^2-r^2)\left\langle\frac{1}{r}\frac{\partial r}{\partial r}\overline{\alpha'\frac{\partial h'}{\partial r}}\right\rangle r\,\mathrm{d}r}_{H_{VI}}\\
&+\underbrace{\frac{16}{\alpha_b(\bar{h}_w-h_b)}\int_0^R (R^2-r^2)\left\langle\frac{\partial}{\partial z}\left(\bar{\alpha}\frac{\partial\bar{h}}{\partial z}\right)\right\rangle r\,\mathrm{d}r}_{H_{VII}}\\
&+\underbrace{\frac{16}{\alpha_b(\bar{h}_w-h_b)}\int_0^R (R^2-r^2)\left\langle\frac{\partial}{\partial z}\left(\overline{\alpha'\frac{\partial h'}{\partial z}}\right)\right\rangle r\,\mathrm{d}r}_{H_{VIII}},
\end{aligned}
\tag{5.15}
$$

where H_I is the laminar, H_{II} is the turbulent and the remaining terms are inhomogeneous contributions to the Nusselt number. The comparison of componential contribution to Nusselt number for $\mathrm{CP}_{K\to\infty}$, $\mathrm{SC}_{K\to\infty}$ and $\mathrm{SC}_{K\to 0}$ are shown in figure 16 (the negligible terms are not shown). As for the skin friction discussed above, the FIK derivation for the Nusselt number is first verified. The sum of all terms is compared with the locally calculated Nusselt number for $\mathrm{CP}_{K\to\infty}$, $\mathrm{SC}_{K\to\infty}$ and $\mathrm{SC}_{K\to 0}$. An excellent agreement is obtained, ensuring correctness and consistency of the derivation (symbols and line overlap). The most significant contributions to the Nusselt number, in terms of relative magnitude, are attributed to the radial turbulent heat flux H_{II}, the laminar part H_I, and the contribution of the mean streamwise enthalpy flux H_{IV}. It is evident that downstream from the inlet, the radial turbulent heat flux H_{II} has the largest contribution to the Nusselt number. The second largest term is the laminar contribution H_I and the term H_{IV} has a positive contribution to Nusselt number at inlet region and it becomes negative further downstream. This is attributed to the growth of the enthalpy profile (thermal boundary layer) and its

product with streamwise velocity. Figure 16(*b*) also shows the influence of different thermal boundary conditions on the componential contributions to the Nusselt number for case $SC_{K\to\infty}$ and $SC_{K\to 0}$. It is evident that the boundary condition solely affects the turbulent radial heat flux H_{II}, thus causing the Nusselt number to reduce for the non-fluctuating wall enthalpy case $SC_{K\to 0}$ by approximately 7 %.

6. Conclusion

In this work we used DNS to investigate the effect of thermal wall boundary conditions on developing turbulent pipe flows with CO_2 at a thermodynamic supercritical pressure of $P_0 = 80$ bar. The Reynolds number based on pipe diameter and inlet friction velocity is $Re_{\tau 0} = 360$ and the inlet Prandtl number is $Pr_0 = 3.19$. Two different wall boundary conditions are studied, namely a case with fluctuating ($SC_{K\to\infty}$) and non-fluctuating ($SC_{K\to 0}$) wall enthalpy. The boundary conditions correspond to the upper and lower limit of thermal effusivity ratio K, respectively. To incorporate both thermal wall boundary conditions, first, a simulation with a constant heat flux boundary condition ($SC_{K\to\infty}$) is performed. Then, for the other simulation, the mean wall enthalpy obtained from the first simulation is used as the thermal wall boundary condition ($SC_{K\to 0}$).

To compare the effects of different thermal boundary conditions on heat transfer to supercritical fluid cases, we also performed DNS with constant property fluids that have the same Reynolds number and Prandtl number as the supercritical fluid cases at the inlet of the pipe. The results show that the wall temperature fluctuations at the wall have very limited effect on the mean enthalpy and Nusselt number for constant property cases. This result is in agreement with existing literature, where it was shown that the Nusselt number is independent of the thermal boundary condition if $Pr \geqslant 1$.

In contrast to the constant property cases, the heat transfer to supercritical fluids with $Pr \geqslant 1$ strongly depends on the thermal wall boundary condition. A significant increase in Nusselt number and bulk enthalpy is observed if thermal fluctuations are allowed at the wall. We found that the wall enthalpy fluctuations cause strong fluctuations in density, viscosity and thermal conductivity, which consequently promote mass and velocity fluctuations that increase turbulent shear stress and turbulent heat flux. A quadrant analysis and FIK identities for both quantities confirms this result, which shows that the turbulent shear stress and turbulent heat flux are attenuated for the non-fluctuating wall temperature case. The present work provides clear evidence that thermal effusivity ratio has a large impact on Nusselt number and skin friction for fluids with large property variations.

Acknowledgements

We acknowledge that the results of this research have been achieved using the PRACE Research Infrastructure resource Cartesius based in The Netherlands at SURFsara. We also wish to thank Dr G. Brethouwer for his comments on an earlier version of the manuscript.

Supplementary movie

Supplementary movie is available at http://dx.doi.org/10.1017/jfm.2016.411.

REFERENCES

BAE, J. H., YOO, J. Y. & CHOI, H. 2005 Direct numerical simulation of turbulent supercritical flows with heat transfer. *Phys. Fluids* **17**, 105104.

BAE, J. H., YOO, J. Y. & MCELIGOT, D. M. 2008 Direct numerical simulation of heated CO_2 flows at supercritical pressure in a vertical annulus at $Re = 8900$. *Phys. Fluids* **20**, 055108.

CARSLAW, H. S. & JAEGER, J. C. 1959 *Conduction of Heat in Solids*, 2nd edn. Clarendon Press.

CHEN, H., GOSWAMI, D. Y. & STEFANAKOS, E. K. 2010 A review of thermodynamic cycles and working fluids for the conversion of low-grade heat. *Renew. Sustainable Energy Reviews* **14** (9), 3059–3067.

CHOI, H., MOIN, P. & KIM, J. 1994 Active turbulence control for drag reduction in wall-bounded flows. *J. Fluid Mech.* **262**, 75–110.

DEBENEDETTI, P. G., TOM, J. W., SANG-DO, Y. & GIO-BIN, L. 1993 Application of supercritical fluids for the production of sustained delivery devices. *J. Control. Release* **24** (1), 27–44.

DOSTAL, V., HEJZLAR, P. & DRISCOLL, M. J. 2006 The supercritical carbon dioxide power cycle: comparison to other advanced power cycles. *Nucl. Technol.* **154** (3), 283–301.

DUAN, L., BEEKMAN, I. & MARTIN, M. 2010 Direct numerical simulation of hypersonic turbulent boundary layers. Part 2. Effect of wall temperature. *J. Fluid Mech.* **655**, 419–445.

FAGES, J., LOCHARD, H., LETOURNEAU, J.-J., SAUCEAU, M. & RODIER, E. 2004 Particle generation for pharmaceutical applications using supercritical fluid technology. *Powder Technol.* **141** (3), 219–226.

FENGHOUR, A., WAKEHAM, W. A. & VESOVIC, V. 1998 The viscosity of carbon dioxide. *J. Phys. Chem. Ref. Data* **27** (1), 31–44.

FUKAGATA, K., IWAMOTO, K. & KASAGI, N. 2002 Contribution of Reynolds stress distribution to the skin friction in wall-bounded flows. *Phys. Fluids* **14** (11), L73–L76.

FUKAGATA, K., IWAMOTO, K. & KASAGI, N. 2005 Novel turbulence control strategy for simultaneously achieving friction drag reduction and heat transfer augmentation. In *Proceedings of the 4th International Symposium Turbulence and Shear Flow Phenomena, Williamsburg, VA, June*, pp. 27–29. Begell House Digital Library.

FUKAGATA, K. & KASAGI, N. 2003 Drag reduction in turbulent pipe flow with feedback control applied partially to wall. *Intl J. Heat Fluid Flow* **24** (4), 480–490.

GOMEZ, T., FLUTET, V. & SAGAUT, P. 2009 Contribution of Reynolds stress distribution to the skin friction in compressible turbulent channel flows. *Phys. Rev.* E **79** (3), 035301.

GOVINDARAJAN, R. & SAHU, K. C. 2014 Instabilities in viscosity-stratified flow. *Annu. Rev. Fluid Mech.* **46**, 331–353.

HETSRONI, G. & ROZENBLIT, R. 1994 Heat transfer to a liquid–solid mixture in a flume. *Intl J. Multiphase Flow* **20** (4), 671–689.

HUANG, P. G., COLEMAN, G. N. & BRADSHAW, P. 1995 Compressible turbulent channel flows: DNS results and modelling. *J. Fluid Mech.* **305**, 185–218.

IRITANI, Y., KASAGI, N. & HIRATA, M. 1985 Heat transfer mechanism and associated turbulence structure in the near-wall region of a turbulent boundary layer. In *Turbulent Shear Flows*, vol. 4, pp. 223–234. Springer.

KAMETANI, Y. & FUKAGATA, K. 2011 Direct numerical simulation of spatially developing turbulent boundary layers with uniform blowing or suction. *J. Fluid Mech.* **681**, 154–172.

KASAGI, N., KURODA, A. & HIRATA, M. 1989 Numerical investigation of near-wall turbulent heat transfer taking into account the unsteady heat conduction in the solid wall. *Trans. ASME J. Heat Transfer* **111** (2), 385–392.

KAYS, W. M. & CRAWFORD, M. E. 1993 *Convective Heat and Mass Transfer*. McGraw-Hill.

KIM, W. S., HE, S. & JACKSON, J. D. 2008 Assessment by comparison with DNS data of turbulence models used in simulations of mixed convection. *Intl J. Heat Mass Transfer* **51** (5), 1293–1312.

KONG, H., CHOI, H. & LEE, J. S. 2000 Direct numerical simulation of turbulent thermal boundary layers. *Phys. Fluids* **12** (10), 2555–2568.

KOREN, B. 1993 *A Robust Upwind Discretization Method for Advection, Diffusion and Source Terms*. Centrum voor Wiskunde en Informatica Amsterdam.

KUNZ, O. & WAGNER, W. 2012 The GERG-2008 wide-range equation of state for natural gases and other mixtures: an expansion of GERG-2004. *J. Chem. Engng Data* **57** (11), 3032–3091.

LEE, J., YOON JUNG, S., JIN SUNG, H. & ZAKI, T. A. 2013 Effect of wall heating on turbulent boundary layers with temperature-dependent viscosity. *J. Fluid Mech.* **726**, 196–225.

LELE, S. K. 1994 Compressibility effects on turbulence. *Annu. Rev. Fluid Mech.* **26** (1), 211–254.

LEMMON, E. W., HUBER, M. L. & MCLINDEN, M. O. 2013 NIST Standard ReferenceDatabase 23: Reference Fluid Thermodynamic and Transport Properties – REFPROP. Version 9.1. Standard Reference Data Program. National Institute of Standards and Technology.

LI, N. & LAIZET, S. 2010 2decomp&fft – a highly scalable 2d decomposition library and fft interface. In *Cray User Group Conference*, pp. 1–13. CUG Conference Proceedings.

LI, Q., SCHLATTER, P., BRANDT, L. & HENNINGSON, D. S. 2009 DNS of a spatially developing turbulent boundary layer with passive scalar transport. *Intl J. Heat Fluid Flow* **30** (5), 916–929.

MA, Y., LIU, Z. & TIAN, H. 2013 A review of transcritical carbon dioxide heat pump and refrigeration cycles. *Energy* **55**, 156–172.

MATSON, D. W., FULTON, J. L., PETERSEN, R. C. & SMITH, R. D. 1987*a* Rapid expansion of supercritical fluid solutions: solute formation of powders, thin films, and fibers. *Ind. Engng Chem. Res.* **26** (11), 2298–2306.

MATSON, D. W., PETERSEN, R. C. & SMITH, R. D. 1987*b* Production of powders and films by the rapid expansion of supercritical solutions. *J. Mater. Sci.* **22** (6), 1919–1928.

MOSYAK, A., POGREBNYAK, E. & HETSRONI, G. 2001 Effect of constant heat flux boundary condition on wall temperature fluctuations. *Trans. ASME J. Heat Transfer* **123** (2), 213–218.

NAJM, H. N., WYCKOFF, P. S. & KNIO, O. M. 1998 A semi-implicit numerical scheme for reacting flow. I: stiff chemistry. *J. Comput. Phys.* **143** (2), 381–402.

NEMATI, H., PATEL, A., BOERSMA, B. J. & PECNIK, R. 2015 Mean statistics of a heated turbulent pipe flow at supercritical pressure. *Intl J. Heat Mass Transfer* **83**, 741–752.

SAKA, S. & KUSDIANA, D. 2001 Biodiesel fuel from rapeseed oil as prepared in supercritical methanol. *Fuel* **80** (2), 225–231.

SPAN, R. & WAGNER, W. 2003 Equations of state for technical applications. I: simultaneously optimized functional forms for nonpolar and polar fluids. *Intl J. Thermophys.* **24**, 1–39.

TENNEKES, H. & LUMLEY, J. 1972 *A First Course in Turbulence*. MIT.

TISELJ, I., BERGANT, R., MAVKO, B., BAJSIC, I. & HETSRONI, G. 2001*a* DNS of turbulent heat transfer in channel flow with heat conduction in the solid wall. *Trans. ASME J. Heat Transfer* **123** (5), 849–857.

TISELJ, I. & CIZELJ, L. 2012 DNS of turbulent channel flow with conjugate heat transfer at Prandtl number 0.01. *Nucl. Engng Des.* **253**, 153–160.

TISELJ, I., POGREBNYAK, E., LI, C., MOSYAK, A. & HETSRONI, G. 2001*b* Effect of wall boundary condition on scalar transfer in a fully developed turbulent flume. *Phys. Fluids* **13** (4), 1028–1039.

VERZICCO, R. & SREENIVASAN, K. 2008 A comparison of turbulent thermal convection between conditions of constant temperature and constant heat flux. *J. Fluid Mech.* **595**, 203–219.

VESOVIC, V., WAKEHAM, W., OLCHOWY, G., SENGERS, J., WATSON, J. & MILLAT, J. 1990 The transport properties of carbon dioxide. *J. Phys. Chem. Ref. Data* **19** (3), 763–808.

YOO, J. Y. 2013 The turbulent flows of supercritical fluids with heat transfer. *Annu. Rev. Fluid Mech.* **45**, 495–525.

ZONTA, F., MARCHIOLI, C. & SOLDATI, A. 2012 Modulation of turbulence in forced convection by temperature-dependent viscosity. *J. Fluid Mech.* **697**, 150–174.